JOURNÉES
DE L'INGÉNIEUR ET DE LA RECHERCHE

Génie Industriel et Logistique
Génie Informatique
Génie Mécatronique

22 & 23 janvier 2024

Livret (1 / 2)

Journée du 22 janvier 2024

Programme

8 H - 9 H

Accueil et inscription

Visite des ateliers, laboratoires, salles et équipements

9 H-9 H 30

Conférence Plénière 1

9 H-9 H 10: Intervention de la direction EPM

9 H 10-9 H 20 : Intervention Représentant de Ecole Polytechnique Saint Louis, France

9 H 20-9 H 30 : Intervention Représentant de Cy Cergy Paris Université, Jean Luc Prigent, France

9 h 30 - 11H 30

Pause

Programme

12H -15H30

Sessions parallèles et Workshops

Workshops 1:

Génie Informatique

Workshops 2:

Génie Mécatronique

Workshops 3:

Génie Industriel et Logistique

15H30 -16H30

Conférence Plénière 2

La recherche à l'EPM

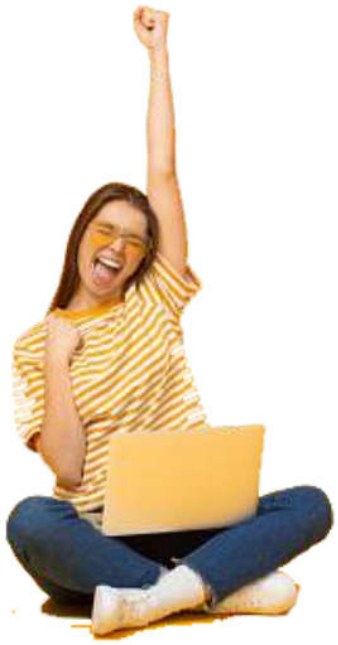

Articles de recherche exposés par les enseignants de l'EPM

ELABORATION AND EVALUATION OF A COMPOSITE BONE SUBSTITUTE BASED ON β-TCP/DCPD AND PHBV, PRELIMINARY RESULTS

Par Dr Monia Trimech

In the present study, we investigate the biological performance of a calcium phosphate ceramics (CPC) bone substitute combined with poly hydroxybutyrate-co-hydroxyvalerate (PHBV). Materials and Methods: A particulate CPC [45% beta-tricalcium phosphate (β-TCP) and 55% of dihydrated dicalcium phosphate (DCPD)] was incorporated into a biodegradable copolymer PHBV. Two series of the composite, 1 and 2, with CPC PHBV weight ratios of (40%–60% and 60%–40%), respectively, were prepared using chloroform for dissolving the polymer and a pressure molding process for shaping the composite samples. After particle size analysis, the two composites were characterized by scanning electron microscopy (SEM) and energy dispersive spectrometry (EDS). In a second step, a 10 mm bony segmental defect created in the tibias of 20 New Zealand White Rabbits was ¯lled randomly with either composite 1 for group 1 or composite 2 for group 2. There were 10 animals in each group. Clinical, radiological and histological assessments were then carried out to evaluate the biological properties of developed CPC–PHBV composites. Results: For both variants of the developed CPC–PHBV biocomposite, there was evidence of osseous consolidation within three months. An in vivo investigation revealed the biological properties of the biocomposite, namely, biocompatibility, bioactivity, biodegradability and osteoconductivity. The morphological characteristics, granule size

---

Sleep-Wake Stages Classification Based on Heart Rate Variability

Par Dr Hayet Wertani

This paper presents a method aimed at classification of the sleep-wake stages using only the electrocardiogram (ECG) records. The feature extraction stage described in this paper was performed using method of Heart Rate Variability analysis (HRV). These features used in this study are based on QRS detection times. Therefore, this detection was generated automatically for all recordings using a new algorithm based on the detection of singularities through the local maxima in order to construct the RR series. We illustrate the

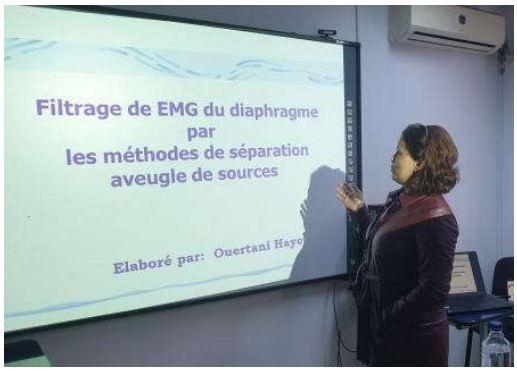

performance of this method on an MIT/BIH Polysomnographic Database using Extreme learning machine (ELM).

Synchronization of the Liu chaotic system and its application in secure communication

Par Dr Hatem Trabelsi

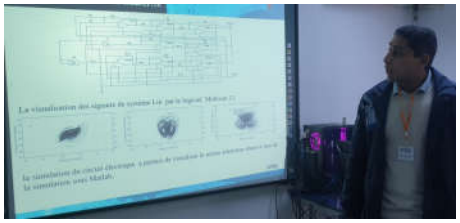

This paper addresses the chaos synchronization of two identical drive-response Liu chaotic systems and its application in secure communication. Based on the vector norm approach, a control law is developed and applied to synchronize both systems' states. The obtained synchronization scheme is implemented using analog circuits and applied for chaos masking communication. Simulation results are presented to demonstrate the effectiveness of the proposed communication system.

Application of the independent components analysis in the reconstruction of acoustic sources in duct systems

Par Dr Raja Dhief

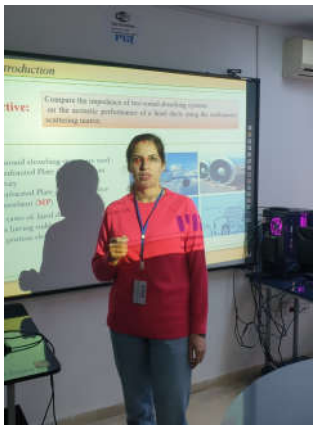

The development of new reconstruction methods of acoustic sources presents a domain of great interest seen its applications in reducing the noise, realizing the acoustic comfort and diagnosing systems. The duct systems are used in several systems such as building, ventilation and aeronautic systems. In this work, a new reconstruction technique of the acoustic sources in duct systems is presented. This technique is based on the multimodal scattering matrix that provides an estimation of the acoustic power dissipation and attenuation in the case of a point acoustic source. These energetic parameters are then injected into an identification technique based on the independent component analysis technique allowing the reconstruction of original sources. The method was applied to a cylindrical rigid-lined-rigid duct element. A comparison between the estimated and imposed acoustic pressures emitted by point sources is presented. This comparison showed that the proposed method gives good results, and the original signals are well reconstructed.

Robust ASR Systems using Auditory Filter in Impulsive Noise Environment

Par Dr Issam Bel Hadj Yahya

This paper is dedicated to the development of new automatic methods for recognizing of isolated words with impulsive sounds. This article presents a parameterization technique of speech signal with impulsive noise based on auditory filter modeling by the gammachirp filterbank (Gammachirp Filter Banc (GFB). This work includes two parts; the first is devoted to traditional techniques. The second deals with modern methods incorporating a model of auditory filter called gamma chirp. In this section, we will extract the characteristics of a single word with impulsive noise from the TIMIT database using parameterization technique Perceptual Linear Prediction (PLP) with the GFB. The recognition system is implemented on

Hidden Markov Model Toolkit HTK platform based on HMM. For evaluation a comparative study was operated with standard PLP and Mel Frequency Cepstral Coefficient (MFCC). We propose a study of the performance of new parameterization technique GFB_PLP and GFB_MFCC proposed in the presence of different impulsive noises. Three types of impulsive noise are used (blast door, glass breaks, and explosion) Tests were carried out at different SNR levels (15dB, 10dB, 5dB, 0 dB and -3 dB) The GFB –PLP technique give the better results in different tests.

Biomedical Engineering: Applications, Basis and Communications, Vol. 28, No. 5 (2016) 1650031 (10 pages)
DOI: 10.4015/S1016237216500319

ELABORATION AND EVALUATION OF A COMPOSITE BONE SUBSTITUTE BASED ON β-TCP/DCPD AND PHBV, PRELIMINARY RESULTS

Monia Trimeche[*,**], Hichem Smaoui[*,†], Ridha Ben Cheikh[*], Mahmoud Smida[‡], Tarek Rebaï[§], Hassib Keskes[¶] and Hassane Oudadess[‖]

[*]*Laboratoire de Matériaux d'Optimisation et d'Energie pour la Durabilité (LAMOED)*
Département Génie Industriel, Ecole Nationale d'Ingénieurs de Tunis
Université Tunis El Manar, Tunisia

[†]*Collège of Engineering*
Prince Sattam bin Abdulaziz University, Kingdom of Saudi Arabia

[‡]*Service d'Orthopédie de l'Enfant et l'Adolescent*
Hôpital d'Enfants de Tunis, Faculté de Médecine de Tunis
Université Tunis El Manar, Tunisia

[§]*Laboratoire d'Histologie Embryologie*
Faculté de Médecine de Sfax, Sfax, Tunisia

[¶]*Unité de Recherche d'Orthopédie-Traumatologie*
Hôpital Habib Bourguiba, Sfax, Tunisia

[‖]*Unité Sciences Chimiques de Rennes*
UMR 6226 CNRS/Université de Rennes 1, Rennes, France

Accepted 27 July 2016
Published 31 October 2016

ABSTRACT

Objective: In the present study, we investigate the biological performance of a calcium phosphate ceramics (CPC) bone substitute combined with poly-hydroxybutyrate-co-hydroxyvalerate (PHBV). **Materials and Methods:** A particulate CPC [45% beta-tricalcium phosphate (β-TCP) and 55% of dihydrated dicalcium phosphate (DCPD)] was incorporated into a biodegradable copolymer PHBV. Two series of the composite, 1 and 2, with CPC–PHBV weight ratios of (40%–60% and 60%–40%), respectively, were prepared using chloroform for dissolving the polymer and a pressure molding process for shaping the composite samples. After particle size analysis, the two composites were characterized by scanning electron microscopy (SEM) and energy dispersive spectrometry (EDS). In a second step, a 10 mm bony segmental defect created in the tibias of 20 New Zealand White Rabbits was filled randomly with either composite 1 for group 1 or composite 2 for group 2. There were 10 animals in each group. Clinical, radiological and histological assessments were then carried out to evaluate the biological properties of developed CPC–PHBV composites. **Results:** For both variants of the developed CPC–PHBV biocomposite, there was evidence of osseous consolidation within three months. An *in vivo* investigation revealed the biological properties of the biocomposite, namely, biocompatibility, bioactivity, biodegradability and osteoconductivity. The morphological characteristics, granule size

[**]Corresponding author: Trimeche Monia, Laboratoire de Matériaux, d'Optimisation et d'Energie pour la Durabilité (LAMOED), Département Génie Industriel, Ecole Nationale d'Ingénieurs de Tunis, Université Tunis El Manar, Tunisia. Tel: 0021697238977; E-mail: monia_trimeche@yahoo.fr

and chemical composition, were indeed found to be favorable for osseous cell development. This study likewise showed lower mortality for the variant with weight ratio (40%CPC–60%PHBV). **Conclusion:** An *in vivo* investigation revealed that the new biomaterial composed of CPC and PHBV exhibits manifest osteoconductivity and bioactivity with better degradation kinetics than the CPC. Moreover, the variant with 40%CPC/60%PHBV appeared more resistant to infection than the 60%CPC/40%PHBV which is an indicator of biocompatibility.

Keywords: Bone substitute; Tissue engineering; Bioceramic; Biopolymer; *In vivo*; Implant.

INTRODUCTION

The reconstruction of bone defects and bone loss has always represented a challenge for orthopedic surgeons. In the past, bone graft was the only known possibility for reconstruction with three origins: human (autograft and allograft) and animal (xenograft).[1]

As it continues to be used worldwide in orthopedic surgery, bone grafting represents today the second most frequent tissue transplantation, after blood transfusion.[2–4] In particular, due to its excellent properties of osteoinduction and osteoconduction, autograft is still considered the "gold standard" of bone reconstruction.

However, many disadvantages, such as post-operative complications, are associated with the application of these grafts.

Autografts are known for their numerous forms of inherent morbidity at the donor site, the occasional prolonged operative time, the unpredictability of graft survival and resorption.[1,2]

On the other hand, allografts undergo various treatments resulting in higher cost and reduced mechanical strength and are known for their limited osteoinduction and the risk of infection. As for xenografts, the risk of transmission of zoonotic diseases discouraged their use in current clinical practice.[2,5,6]

These drawbacks motivated the development of substitutes for natural bone. During the past 50 years, materials research and tissue engineering have witnessed the emergence of a variety of biocompatible materials of synthetic and natural origins. Synthetic bone substitutes are designed and developed such that they exhibit the required characteristics of biodegradability, bioactivity and mechanical resistance.[3,4,7]

Bioresorbable bone substitutes are most commonly made out of calcium phosphate ceramics (CPC) or biopolymers owing to their suitable properties.[8]

CPC are bioresorbable and exhibit satisfactory mechanical strength in addition to their excellent biocompatibility and bioactivity.[9] For example, tricalcium phosphate (β-TCP) is particularly known for its bioresorbability and dicalcium phosphate dihydrate is precursor of osseous mineralization.

Poly-hydroxybutyrate-co-hydroxyvalerate (PHBV), a copolymer of poly-hydroxybutyrate with varying ratios of hydroxyvalerate, is a biocompatible and biodegradable biopolymer with appropriate degradation rates.[9] Having a ductile behavior, its blinding with ceramic eliminates the intrinsic brittleness of the later.

However, some drawbacks are associated with the use of CPC or biopolymers as bone substitutes. For instance, the kinetics of degradation of CPC is inappropriately fast for bone growth and its compressive strength after biodegradation has been reported to be in the range of 70–80 MPa[27] which is by far superior to that of normal cancellous bone estimated to be 14.6 MPa.[27]

As for PHBV, it is limited in bioactivity and, consequently, it does not bond tight enough with the newly formed tissue.[10]

Interestingly, it happens that for each of the desired properties, at least one of the two biomaterials exhibits satisfactory performance. By combining them in appropriate proportions, biocomposites could be produced that outperformed both constituents as bone substitute materials.[10,11] As an example, Cool *et al.*[12] showed that adding various forms of CPC, namely, hydroxyapatite, calcined hydroxyapatite or β-TCP, to a PHBV matrix reduced the inflammatory manifestations of the latter while improving its bioactivity and mechanical properties.

In the present study, we aimed at developing and assessing the essential bone regeneration characteristics of a biocomposite bone substitute consisting of the combination of the biopolymer PHBV with a CPC that is currently used in orthopedic practice. The latter, composed of 45% TCP and 55% dihydrated dicalcium phosphate (DCPD), is characterized by the fast degradation kinetics that is typical for CPC products. In the literature there is no work involving (45% β-TCP, 55% DCPD) with PHBV in a composite bone substitute.

MATERIALS AND METHODS

In order to identify a composition of the CPC–PHBV biocomposite that is suitable for orthopedic applications

two series of samples were prepared with two different CPC–PHBV weight ratios (40%/60% and 60%/40%). These ratios were chosen to be reciprocals, that is, symmetric, for the sake of objectivity. The particle size was classified using a vibrating screen. The morphology and the chemical composition in elements were analyzed by using a high-resolution microscope, scanning electron microscopy and energy dispersive spectrometry (SEM–EDS).

Then, to determine the most suitable weight ratio for osseous repair, the biocomposite samples were implanted bone defects created in Rabbit tibias. Radiographic and histological observations were conducted to obtain a preliminary assessment of the performance of each variant of the biocomposite.

Manufacture of Materials

The raw materials used for the development of the proposed biocomposite were a PHBV copolymer and the CPC. The PHBV component was manufactured in the form of small size pellets by Tianan® (Emmat-Y1000P). Its general chemical formula is given in Fig. 1.[13]

The CPC component was composed of 45% TCP and 55% of DCPD. It is commercially available in the form of fine white powder with a porosity of 40% according to the manufacturer (KASIOS®, France).

Composite Production Protocol

The CPC–PHBV composite was prepared using a molding process (Fig. 2). Two series of samples were prepared with two CPC–PHBV ratios (40%–60% and 60%–40%).

For adequate dispersion of CPC in the PHBV matrix, the mixture was poured into a solution of chloroform (ScienTEST®. Germany) with 5 g of mixture/200 mL and heated for 2 h at 80°C with stirring at constant speed. Then evaporation was applied using a rotary evaporator (Stuart®) for effective removal of solvents. Finally, the precipitate was dried for 24 h in an oven at 100°C, ground, crushed in an electric crusher and then compressed into pellets of 1 cm diameter and 1 cm thickness using a pelletizer (Fig. 2).

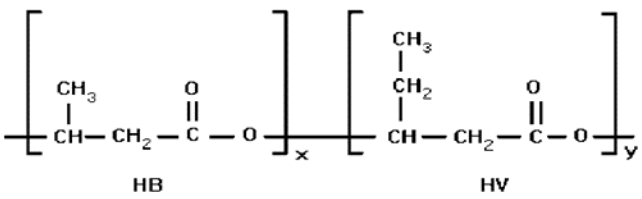

Fig. 1 Chemical formula of PHBV.

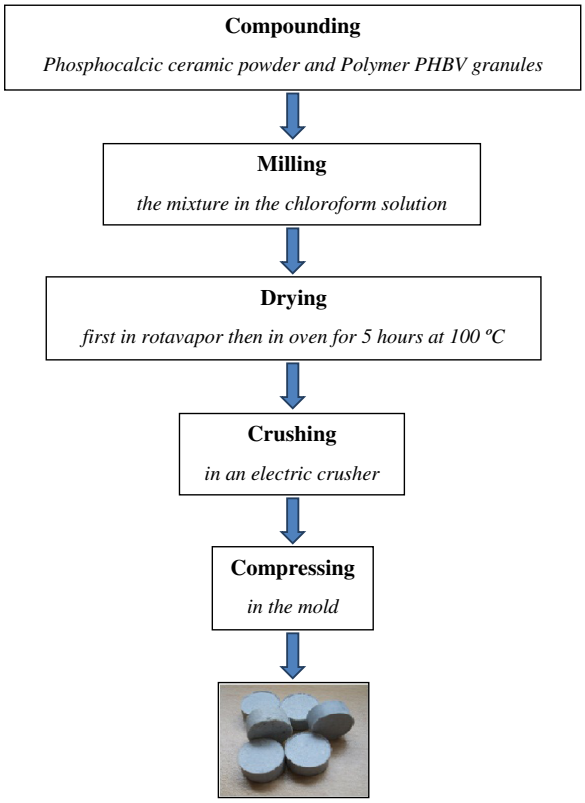

Fig. 2 Elaboration process of bioceramic-polymer composite.

Characterization of the Composite

Physico-chemical characterization of the biomaterial was carried out to evaluate the properties that influence its biocompatibility such as chemical composition, surface characteristics and particle size.

Particle size analysis

The particles of CPC–PHBV were placed in a vibrating sieve and were subjected to continuous vibration for 30 min. Six sieves of successive stitches: 100, 160, 200, 400, 600 and 800 were used, which fully covered the actual range of particle sizes.

SEM–EDS analysis

The SEM–EDS analysis was conducted to observe the morphology and the distribution of the ceramic within the polymer matrix. The microanalyses were carried out with the SEM Jeol JSM 6400, equipped with an Oxford Link INCA spectrometer of energy dispersion.

The spectral analysis of each sample gives the mass percentage of chemical elements detected in each spectrum.

In vivo Evaluation of Composite

Animal model

In this study, the experiments were performed on 20 skeletally mature male New Zealand white male rabbits weighing 1.8–2.2 kg. To keep the animals healthy before undergoing surgery, they were placed in separate cages during one week under suitable and carefully controlled conditions in terms of cleanliness, temperature, humidity and nutrition.

The implantation of the biomaterial was performed randomly on a group of 10 rabbits for each of the two compositions. Groups 1 and 2 were implanted with samples from series 1 (40% CPC–60% PHBV) and 2 (60% CPC–40% PHBV), respectively.

Operative procedures

The CPC–PHBV pellets were sterilized by γ-irradiation from a ^{60}Co gamma irradiation source at a dose of 25 Gy (Equinox, UK) using standard procedures for medical devices.

The surgical procedure earned approval from the ethical committee of the Tunisian Association of Laboratory Animal Sciences (*www.atsal.org*) according to the ICLAS ethical guidelines for researchers (*www.iclas.org/committee/ethics-and-animal-welfare-committee*).

All animals were subject to general, backed with local, anesthesia through intramuscular administration of 10 mg/kg ketamine hydrochloride (Ketaminol®, Germany) and 0.1 mg/kg xylazine (Rompun®, France). In each animal, one lower limb was prepared aseptically for surgery. After shaving the lower limb segment and disinfecting it with Betadine®, a 4 cm skin incision was made medially over the leg and the tibia was exposed subperiosteally. A 10 mm bony segmental defect was then created by two osteotomies in the middle portion of the tibia. The osteotomy was performed with an oscillating saw at a right angle to the axis of the bone. The defect was then, filled with a suitably shaped composite sample (Fig. 3).

To stabilize the tibia and maintain a direct contact between composite and bone, a mini-stainless steel monoplanar external fixator was used. Four pins were inserted through the skin into the bone and then attached to a steel rod outside the limb (Fig. 3). Next, the wound was closed for the periosteum and the subcutaneous tissues using a resorbable suture. Finally, a post-operative bandage was made with a sterile compress after local application of Betadine® gel.

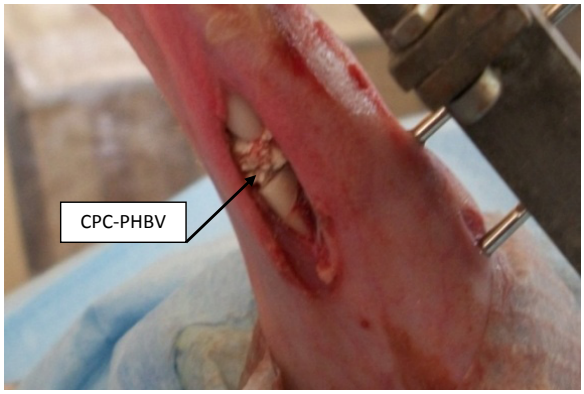

Fig. 3 CPC–PHBV implanted in the tibia of a rabbit.

Clinical assessment

In the post-operative period, daily clinical controls of the operated animals were made. The first dressing was changed on the third post-operative day. The wounds were controlled on a daily basis. They were inspected locally and cleaned using a physiological serum and Betadine® gel to prevent surgical site infection and external microbial transfer. This should protect from internal inflammatory reactions that may appear during the first week following surgery. The skin suture was removed on the 15th post-operative day after wound healing.

Radiological evaluation

To assess the stability of the composite and follow the general structural health of the operated bone, anteroposterior and lateral radiographs of each operated leg were made on the second day of the osteotomy. We also took serial radiographs at the first, second and fourth post-operative week and finally, at the third post-operative month.

Histological Evaluation

To evaluate composite osteointegration and the biological response of the bone tissue in contact, histological studies were conducted at various times after the implantation.

Two operated animals of every group were sacrificed 30 days after surgery. The remaining rabbits were sacrificed after 90 post-operative days. The operated leg of each animal was harvested and dissected free of soft tissues. The recuperated tibia was fixed in 10% formaldehyde during 24 h to immobilize the cells for

subsequent histological studies. The timing was selected to assess the performance of the biomaterial bone formation before degradation. The samples were then dehydrated in three successive acetone baths. Next, they were placed in methyl methacrylate (MMA) without prior decalcification. Sections 6–7 μm thick were debited along a transverse plane using a sliding microtome (Reichert-Jung).

Once colored with Goldner's Masson trichrome, hematoxylin-phloxine or blue toluidine–borax–eosin, the cut was mounted between slide and slip cover.

The colored cuts were observed through a binocular microscope (Olympus® CX-21i) and the observations were photographed with various magnifications using the digital camera (Nikon® E 950) assembled onto the microscope.

RESULTS

Composite Characterization

The particle size distribution is shown in Fig. 4 for the 40/60 and 60/40 compositions of the CPC–PHBV biomaterial. In the 40/60 composite most particles (had diameters between 200 and 600 (μm) whereas in the 60/40 composite the majority (98%) of particles were in the range of 160–600 μm. However, the particle size of CPC was in the interval 63–200 μm. The CPC used in this study was available in the form of a fine, white, crystalline powder (Fig. 5). It was composed of four chemical elements: calcium, phosphorus, oxygen and hydrogen (Table 1). It should be noted that the hydrogen element cannot be detected because in front of the MEB detector, a "window" prevents the passage of the photons of low energies.

The morphology was similar for the two tested variants (40/60 and 60/40) of the CPC–PHBV biocomposite. It is characterized by a porous structure with interconnected pores (Fig. 7), sharp edges, irregular profile and rough surface with microcracks (Fig. 6).

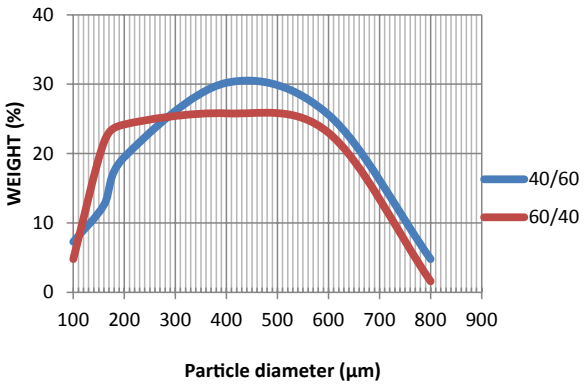

Fig. 4 Particle size distribution of CPC/PHBV.

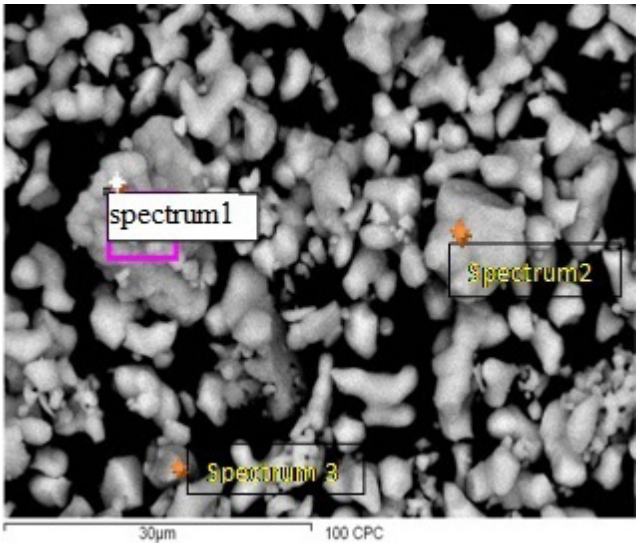

Fig. 5 SEM micrographs of CPC.

Table 1. Distribution of Mass Components of CPC.

	(CPC), % Weight		
Atom	**Spectrum: 1**	**Spectrum: 2**	**Spectrum: 3**
O_K	50.43	41.07	37.35
P_K	22.12	21.51	21.36
Ca_K	27.45	37.42	41.29

Clinical Control

Once introduced into the bone, the CPC–PHBV composite triggered, like any other foreign body, a transitory

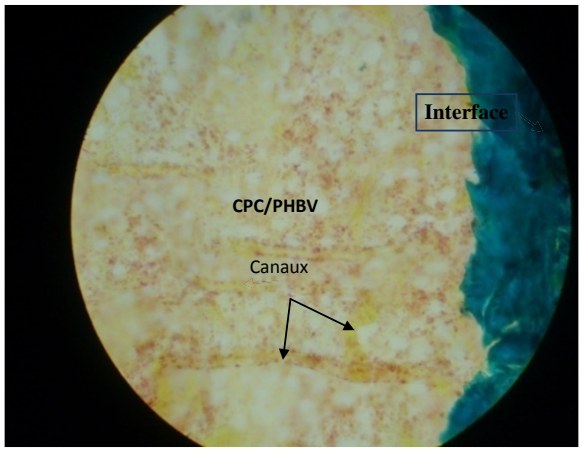

Fig. 6 (Color online) Longitudinal section shows a porous interconnected architecture (arrows) of composite (40/60) (yellow color) and a strong cohesion at the interface with tibia bone (blue). Trichrome Goldner, (Magnification 60X).

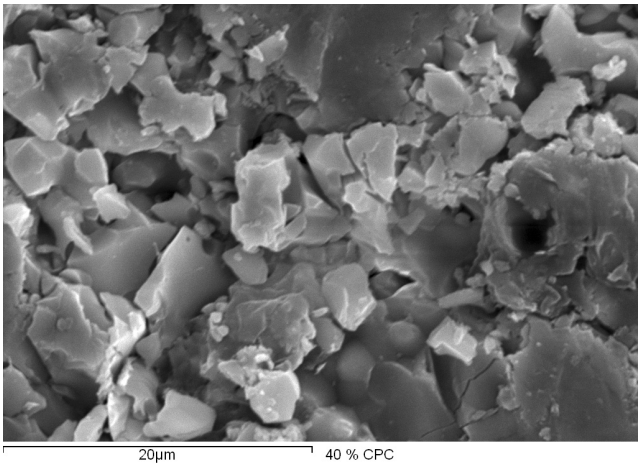

Fig. 7 SEM micrographs of CPC–PHBV (40–60) surface, showing sharp edges and porous structure. CPC/PHBV 40/60.

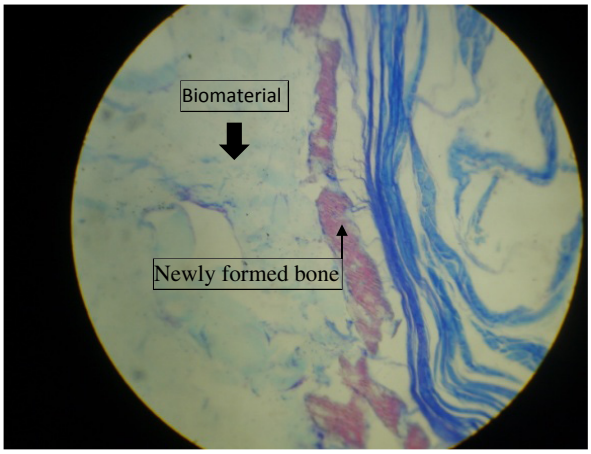

Fig. 9 (Color online) Longitudinal cut of an osseous sample showing the newly formed bone on the biomaterial surface (purple color). Toluidine blue–Borax–Eosine staining, (Magnification 60X).

inflammatory reaction. During the post-operative period, the daily clinical evaluation exhibited no sign of surgical site infection (i.e. swelling, redness or wound disunion) on the operated rabbits which had overcome the tibial osteotomy.

As for the others, three rabbits in group 2 (60/40) and two in group 1 (40/60) died in the first post-operative week and were therefore excluded from the study. Through careful evaluation during the pre-mortem period and checking for post-operative complications, we noted decreased food and water intake by these rabbits, increase in respiration, aggressiveness and reduced mobility.

At 10 post-operative weeks, two other rabbits died in group 2, reducing the survival rate to 50%, while it remained at 80% in the other group.

Radiological Findings

At 12 post-operative weeks, the radiographs showed complete healing of the host bone and disappearance of the implanted biomaterial (Fig. 8). In fact, bone consolidation was noted in six rabbits out of eight in group 1 and two rabbits out of five in group 2.

Microscopic Evaluation

The microscopic observations have shown that the CPC–PHBV composite stimulated a bone regeneration process. This was manifested by the formation of a mineralized layer on the surface biomaterial (Fig. 9).

Bone forming cells appeared in some histological sections. Figure 11 shows the osteoclasts that are responsible for bone resorption. Osteoblasts and osteocytes are shown in Fig. 11.

Fig. 8 Radiographs of bone remodeled after 12 weeks.

DISCUSSION

With the growing social requirements and aging populations, the orthopedic surgeons are increasingly confronted with bone losses and defects of different origins. When the segmental bone defect is large, the bone fails to reconstruct itself. Natural bone grafts have long been applied in bone reconstruction. The limitations and complications associated with these grafts (inherent morbidity, unpredictability of graft survival and resorption, higher cost and reduced mechanical strength, limited osteoinduction and risk of infection, non-availability) motivated the development of synthetic bone substitutes exhibiting the desired properties that were deficient in natural bone grafts.

In the last decades, natural and synthetic bone substitutes emerged that satisfy several essential criteria for bone regeneration. These include biocompatibility, bioactivity, osteoinductivity, osteoconductivity and biodegradability, the latter being correlated with new bone formation.[14–16]

Bone substitute materials commonly consist of polymers, ceramics or composites thereof. Calcium phosphates, a major class of bioceramics, are biocompatible, biodegradable and bioactive, which makes them well suited for bone substitution. Their osteoconductivity

stimulates bone formation by favoring attachment, migration and differentiation of bone cells.

PHBV, a widely used biopolymer, is favored for its suitable degradation rates[12] while being biocompatible. Actually, this biomaterial is easily produced. Furthermore, PHBV polymers can be used as temporary extracellular matrices in composite bone substitutes.[11,17,18]

Researchers have believed that the original structure of natural bone could be synthetically reproduced.[19,20] In fact, the pair formed by polymeric matrices and ceramics simulates the two components of natural bone, organic collagen and inorganic HAP.[21]

In this study, we chose a CPC commercially named JECTOS to be incorporated in a polymeric matrix. It is composed of β-TCP and DCPD. The former component has an excellent osteoconduction capacity. Furthermore, it has an alkaline nature. It therefore constitutes a preferred component for hybrid and composite scaffolds to be combined with polymers. The second component is utilized as a precursor of osseous mineralization.[22]

Currently, the CPC product is routinely utilized alone for bone repair. Orthopedic surgeons have generally found that it disappears prematurely in the site, before bone growth is completed. Combining it with the PHBV was expected to convey to the composite some of the desirable properties for the bone substitute, that is, to slow down the resorption kinetics of the CPC and to gain some ductility. The fineness of its particles (63–200 μm) should ease their integration into the polymer matrix.

Two variants of CPC–PHBV were elaborated with different weight ratios: 40/60 and 60/40. These ratios were chosen to be reciprocals, that is, mutually symmetric, for the sake of objectivity. The smaller ratio was set to 40% so that the amount of the component with the smallest fraction be sufficient to convey its desirable properties to the composite. At the present stage of the study, the characteristics of the limit compositions consisting of either CPC or PHBV alone were based on sources from the literature.

Given the closeness of the metabolism of rabbits to humans', we estimated that the resorption kinetics in rabbits can fairly be assumed to be similar to that in humans.

First, we studied the particle size which is a determining factor in the kinetics of degradation. The particle size range (100–800 μm) of the proposed CPC–PHBV was practically the same for both variants.

The occurrence of bone rebuilding, in the *in vivo* study, for at least one subject in each of the two operated groups is indicative of the adequacy of the particle size distribution and the resorption kinetics of both composites. Then, we can deduce that the particle size of CPC–PHBV is optimal, their dissolution kinetics had not delayed the bone regeneration so, their resorption rate was appropriate for new bone formation. Therefore, a particle size between 100 and 800, is adequate with the request resorption kinetics. In literature, there was not a particular size for grains of bone substitute; this is due to the distinction of products and technical elaborations of biomaterials. Besides, several existing studies in the literature are contradictory.[23,24]

As a preliminary, we analyzed the particle size which is a determining factor in the kinetics resorption. In literature, there was no definite recommendation for grain size of bone substitutes. Besides, several studies in the literature are contradictory.[23,24] This is due to the variety of products and technical elaborations of biomaterials.

The particle size range (100–800 μm) of the proposed CPC–PHBV was practically the same for both variants. The occurrence of bone rebuilding for at least one subject in each of the two groups, with bone regeneration continued until completion of consolidation, is indicative of the adequacy of the resorption kinetics and the particle size for new bone formation. It may be concluded that, for the proposed biocomposite, a particle size range between 100 and 800 μm, is consistent with a good resorption kinetics.

Nevertheless, there seems (Table 1) to be enough calcium and phosphate ions to drive the necessary chemical interactions with the biological structure in contact.

The CPC–PHBV composites had an irregularly shaped microporous architecture (Fig. 6). Under favorable conditions, these pores constitute a microenvironment for cell adhesion and proliferation.[25,26] The microcracks that appear on the composite surfaces (Fig. 6) can also serve as lodging for cell multiplication. Both composites had surfaces with a rough appearance which reveals a structure that favors osteoblastic differentiation.

The *in vivo* investigation brought us insight on the bone response to the implants and, hence, on the biological properties of the biomaterials. It should be noted that the biomaterial with weight ratio (40/60) exhibited the best result in terms of number of restored rabbits in 90 days. While various factors besides poor biocompatibility may potentially cause infection, clinical control suggests that the biomaterial 40/60 is more biocompatible than 60/40. Indeed, in group 1, no symptoms of infection were detected, while for group 2 necrosis signs were observed on the members of two rabbits which eventually died after achieving some progress in the

regeneration. Furthermore, histological sections showed evidence of osteointegration of the CPC–PHBV. A strong cohesion between the 40/60 biocomposite and the bone is seen in Fig. 7.

The gradual occupation of CPC–PHBV substitute by a differentiated tissue requires resorption thereof. This process needs a combination of biological properties to be achieved. The first is the biodegradability leading to the disappearance of the biomaterial (Fig. 12). The second is the osteogenesis which reflects the construction of the bone matrix by the bone cells. This cellular activity is deduced from Figs. 10 and 11. Figure 10 shows an osteoclast cell whereas, in Fig. 11, the osteoblast cells are arranged on the periphery of the biomaterial and the osteocytes are trapped inside the bone matrix.

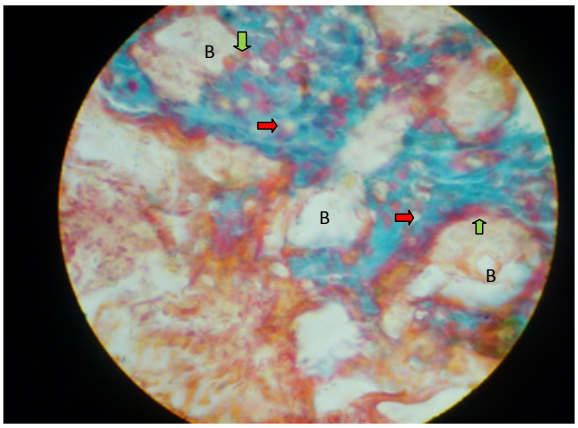

Fig. 10 (Color online) Transversal cut of an osseous sample showing mineralized newly formed tissue (blue) and osteoblasts (green arrow), surrounding the biomaterial (B) (60/40) and osteocytes (red arrow), (four weeks of implantation), hematoxylin-phloxine staining, (100X).

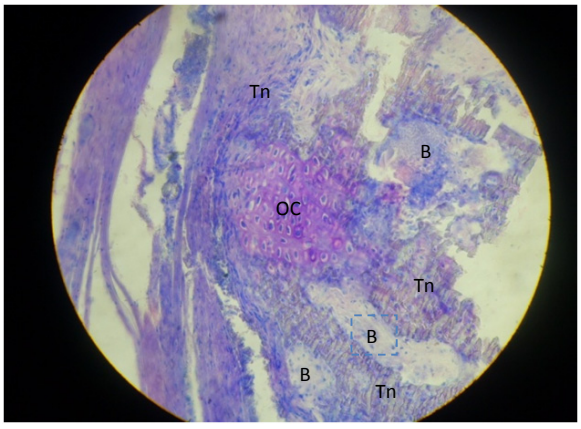

Fig. 11 Longitudinal section showing a newly formed tissue (Tn) surrounding the biomaterial (40/60) (B) and osteoclast (OC) in the center. (eight weeks of implantation), hematoxylin-phloxine stain, (100X).

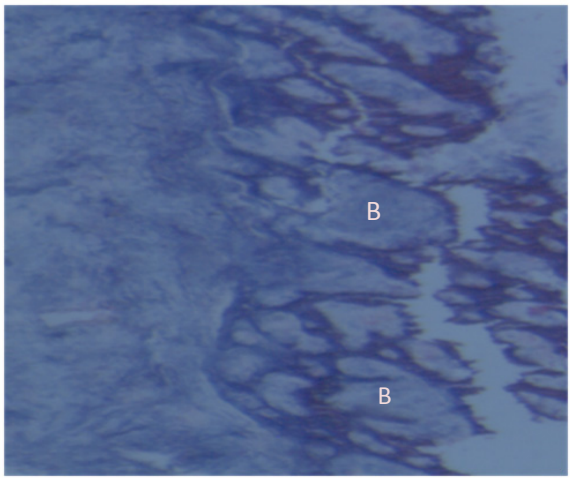

Fig. 12 Transversal cut of (40/60) CPC/PHBV (B) in degradation stage (eight weeks implantation), blue toluidine–borax–eosinestaining, (Magnification 100X).

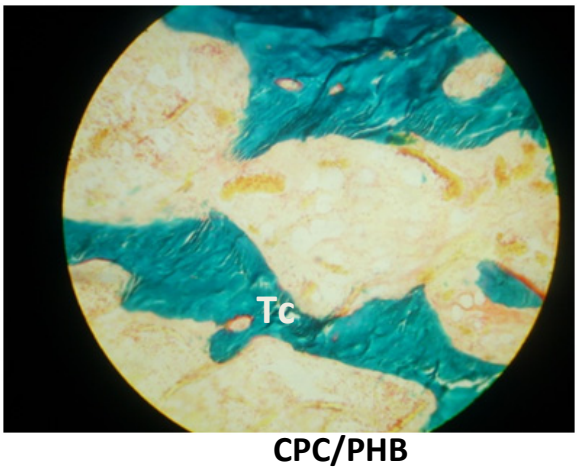

Fig. 13 (Color online) Longitudinal section showing a calcified tissue (blue) covered the space left by the biodegradation of 40% CPC/60% PHBV, (four weeks). Trichrome Goldner, (100X).

Osteoconduction of the composite is demonstrated by the histologic sections (Figs. 10, 11 and 13) extracted from the middle of the implanted site away from the periphery where bone growth initiates. The figures show formation of bone tissue where the bone could not possibly exist if the biomaterial were not osteoconductive.

CONCLUSION

A β-TCP/DCPD bioceramic routinely used as bone substitute has been combined with PHBV for the purpose of producing a biocomposite with superior biological properties. Two variants of CPC/PHBV bone implants containing 40% and 60% by weight of bioceramic have been manufactured and investigated.

Morphological analysis, chemical identification and a preliminary *in vivo* experimentation on New-Zealand rabbits were conducted. The results provided evidence of biocompatibility, biodegradability, osteoconductivity and bioactivity. The kinetics of biodegradability of the composite is revealed to be more appropriate than that of the CPC. The higher survival rate observed in the cohort implanted with 40% CPC–60% PHBV composition *a priori* suggests better biocompatibility and, consequently, better potential for bone repair than with 60% CPC–40% PHBV. An extended *in vivo* investigation with control groups including sham-operated and control-implanted with exclusively CPC will next be performed together with a mechanical characterization in order to draw firm conclusions on the merits of the proposed composite.

An *in vivo* investigation revealed that the new biomaterial composed of CPC and PHBV exhibits manifest osteoconductivity and bioactivity with better degradation kinetics than the CPC. Moreover, the variant with 40% CPC/60% PHBV appeared more resistant to infection than the 60% CPC/40% PHBV which is an indicator of biocompatibility.

ACKNOWLEDGMENT

I thank the University of Rennes 1, France and the University of Sfax, Tunisia.

REFERENCES

1. Beaman FD, Bancroft LW, Peterson JJ, Kransdorf MJ, Bone graft materials and synthetic substitutes, *Radiol Clin North Am* **44**:451–461, 2006.
2. Campana V, Milano G, Pagano E *et al.*, Bone substitutes in orthopaedic surgery: From basic science to clinical practice, *J Mater Sci Mater Med* **25**:2445–2461, 2014.
3. Finkemeier CG, Bone-grafting and bone-graft substitutes, *J Bone Joint Surg* **84-A**:454–464, 2002.
4. Greenwald AS, Boden SD, Goldberg VM *et al.*, Bone-graft substitutes: Facts, fictions and applications, *J Bone Joint Surg* **83-A**:98–103, 2001.
5. Fowler BL, Dall BE, Rowe DE, Complications associated with harvesting autogenous iliac bone graft, *Am J Orthop* **24**:895–903, 1995.
6. Lofgren H, Johannsson V, Olsson T, Ryd L, Levander B, Rigid fusion after Cloward operation for cervical disc disease using autograft, allograft, or xenograft: A randomized study with radiostereometric and clinical follow-up assessment, *Spine* **25**:1908–1916, 2000.
7. Gazdag AR, Lane JM, Glaser D, Forster RA, Alternatives to autogenous bone graft: Efficacy and indications, *J Am Acad Orthop Surg* **3**:1–8, 1995.
8. Arner JW, Santrock RD, A historical review of common bone graft materials in foot and ankle surgery, *Foot Ankle Spec* **7**:143–151, 2014.
9. Rezwan K, Chen QZ, Blaker JJ, Boccaccini AR, Biodegradable and bioactive porous polymer/inorganic composite scaffolds for bone tissue engineering, *Biomaterials* **27**:3413–3431, 2006.
10. Chen LJ, Wang M, Production and evaluation of biodegradable composites based on PHB–PHV copolymer, *Biomaterials* **23**:2631–2639, 2002.
11. Asefnejad A, Behnamghader A, Khorasani MT, Farsadzadeh B, Polyurethane/fluor-hydroxyapatite nanocomposite scaffolds for bone tissue engineering. Part I: morphological, physical, and mechanical characterization, *Int J Nanomed* **6**:93–100, 2011.
12. Cool SM, Kenny B, Wu A, Nurcombe V, Trau M, Cassady AI, Grøndahl L, Poly(3-hydroxybutyrate-co-3-hydroxyvalerate) composite biomaterials for bone tissue regeneration: *In vitro* performance assessed by osteoblast proliferation, osteoclast adhesion and resorption, and macrophage proinflammatory response **82**(3):599–610, 2007.
13. Köse GT, Kenar H, Hasirci N, Hasirci V, Macroporous poly(3-hydroxybutyrate-co-3-hydroxyvalerate) matrices for bone tissue engineering, *Biomaterials* **24**:1949–1958, 2003.
14. Danoux CB, Barbieri D, Yuan H, de Bruijn JD, van Blitterswijk CA, Habibovic P, In vitro and *in vivo* bioactivity assessment of a polylactic acid/hydroxyapatite composite for bone regeneration. *Biomatter* **4**:e27664, 2014.
15. Gogolewski S, Jovanovic M, Perren SM, Dillon JG, Hughes MK, Tissue response and *in vivo* degradation of selected polyhydroxyacids: Polylactides (PLA), poly(3-hydroxybutyrate) (PHB), and poly(3-hydroxybutyrate-co-3-hydroxyvalerate) (PHB/VA), *J Biomed Mater Res* **27**:1135–1148. 1993.
16. Cao H, Kuboyama N, A biodegradable porous composite scaffold of PGA/beta-TCP for bone tissue engineering, *Bone* **46**:386–395, 2010.
17. Jack KS, Velayudhan S, Luckman P, Trau M, Grøndahl L, Cooper-White J, The fabrication and characterization of biodegradable HA/PHBV nanoparticle-polymer composite scaffolds, *Acta Biomater* **5**(7):2657–2667, 2009.
18. Liu, Y, Wang, M, Thermophysical and mechanical properties of β-tricalcium phosphate reinforced polyhydroxybutyrate and polyhydroxybutyrate-co-hydroxyvalerate composites, *Eng Mater* **334**–**335**:1217–1220, 2007.
19. Bhumiratana S, Grayson WL, Castaneda A, Rockwood DN, Gil ES, Kaplan DL, Vunjak-Novakovic G, Nucleation and growth of mineralized bone matrix on silk-hydroxyapatite composite scaffolds, *Biomaterials* **32**:2812–2820, 2011.
20. Wang M, Developing bioactive composite materials for tissue replacement, *Biomaterials* **24**:2133–2151, 2003.
21. Wei G, Ma PX, Structure and properties of nano-hydroxyapatite/polymer composite scaffolds for bone tissue engineering, *Biomaterials* **25**:4749–4757, 2004.
22. Roufosse AH, Landis WJ, Sabine WK, Glimcher MJ, Identification of brushite in newly deposited bone mineral from embryonic chicks, *J Ultrastruct Res* **68**:235–255, 1979.

23. Malard O, Bouler JM, Guincheux J, Heymann D, Pilet P, Influence of biphasic calcium phosphate granulometry on bone ingrowth, ceramic resoption and inflammatory reactions: Preliminary *in vitro* and *in vivo* study, *J Biomed Mater Res* **46**:103–111, 1999.
24. Malard O, Etude des céramiques phosphocalciques de substitution osseuse en territoire irradié: intérêt d'une autogref, Universite de Nantes, Faculte de Chirurgie Dentaire: Sciences de la vie et de la santé, Nantes, 2004.
25. Habibovic P, Kruyt MC, Juhl MV, Clyens S, Martinetti R, Dolcini L, Theilgaard N, van Blitterswijk C, Comparative *in vivo* study of six hydroxyapatite-based bone graft substitutes, *J Orthop Res* **26**(10):1363–1370, 2008.
26. Zhu XD, Fan HS, Xiao YM, Li DX, Zhang HJ, Luxbacher T, Zhang XD, Effect of surface structure on protein adsorption to biphasic calcium-phosphate ceramics *in vitro* and *in vivo*, *Acta Biomater* **5**(4):1311–1318, 2009.
27. Kasuya, A, Sobajima S, Kinoshita M, *In vivo* degradation and new bone formation of calcium phosphate cement–gelatin powder composite related to macro-porosity after in situ gelatin degradation, *J. Orthop. Res.* **30**:1103–1111, 2012, doi: 10.1002/jor.22044.

Sleep-Wake Stages Classification Based on Heart Rate Variability

Werteni Hayet
Signal, Image and information technology laboratory
ENIT BP 37, 1002, Belvédère, Tunisia
hayet_werteni@yahoo.fr

Yacoub Slim
INSAT, Dept. Of Physique and Instrumentation,
BP 676,1080, Centre Urbain, Tunisia
Slim.yacoub@insat.rnu.tn

Abstract—**This paper presents a method aimed at classification of the sleep-wake stages using only the electrocardiogram (ECG) records. The feature extraction stage described in this paper was performed using method of Heart Rate Variability analysis (HRV). These features used in this study are based on QRS detection times. Therefore, this detection was generated automatically for all recordings using a new algorithm based on the detection of singularities through the local maxima in order to construct the RR series. We illustrate the performance of this method on an MIT/BIH Polysomnographic Database using Extreme learning machine (ELM)**.

Keywords-ECG, Heart rate variability, sleep stages, Exterme learning machine.

I. INTRODUCTION

During the past years, the assessments of sleep become an important issue by reason the considerable number of pathologies associated with sleep periods. Therefore, a good analysis of sleep was presented with a classification of the night stages. For this reason, a polysomnography (PSG) was done; which is a reference test for quantifying and qualifying sleep disorders. It is presented by the recording of several physiological variables during the night's sleep [1], in order to classify the different phases of sleep. These variables was: the electro-encephalogram (EEG), electro-oculogram (EOG), electro-myogram (EMG), respiratory effort, air flow entering through nose and mouth, the saturation of oxygen in hemoglobin, the electro-cardiogram (ECG) and effort of the thoracic and abdominal muscles. ECG recording is one of the simple technologies in sleep disorders detection. Cyclic variations in RR intervals of ECG signals have been reported to be associated with sleep apnea and different sleep stages [2]. Various studies have confirmed that several methods could possibly recognize the stages of sleep from the ECG signal. All these studies was based on analysis of RR interval variability, which present the variation in time period between consecutive heart beats and gives a measure of the modulation of sympathetic and parasympathetic nervous system. During sleep, the study of this variability can show the modification of the cardiovascular system regulation based on sleep cycles [3]. Several studies [4], [5] were investigated in blood pressure changes of breathing with the sleep depth, and showed significant differences in parameters of heart rate variability during all stages of sleep. Recently, new approaches have emerged [6], [2], [7] and [8] which classified sleep stages based only on the RR interval, which used in the extraction phase detrended fluctuation analysis (DFA), the analysis of heart rate variability analysis (HRV) and windowed detrended fluctuation analysis (PDFA)

This paper is concerned by sleep wake stages classification based on heart rate variability, and is organized in four parts. Section 2 present: the MIT/BIH polysomnographic Database, processing of the signal ECG, the feature extraction method and the classification algorithm. Section 3 pesent the Classification results. Finally conclusions are presented in Section 4.

II. METHODS

In this study, ECG epochs were classified in one of two categories “Awake” and “Sleep” .The classification system used in this paper consists of three steps: firstly a preprocessing is applied on the ECG signal in order to build the RR series, then, the feature extraction. Finally, we adopt the Extreme Learning Machine for the classification phase. The block diagram of the proposed classification method is illustrated in Fig. 1.

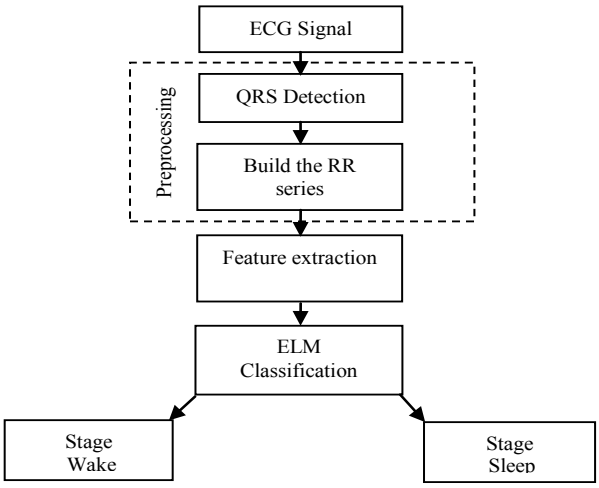

Figure 1. Diagram of classification algorithm

A. MIT/BIH Polysomnographic Database

The approach presented in this paper is tested using ECG registrations from the MIT-BIH polysomnographic database. This database is a collection of recordings of multiple physiologic signals during sleep with sampling rate 250Hz.

The database contains over 80 hours' worth of four-, six-, and seven-channel polysomnographic recordings, each with specifically an ECG signal annotated beat-by-beat. The 16 patients (16 males aged 32 to 56) in this database suffer from a condition known as sleep apnea in which they are repeatedly awoken during the night due to their breathing being interrupted [9].

The data files contain the header file, the QRS annotations file and the sleep stages file. The header file is a text file containing the information related to the record such as, the types of the signals, calibration constants, the length of recordings, and the anthropometric data of the subject. The QRS annotations give the time occurrence of each QRS complex, whereas sleep stages file contains the class label of each epoch, i.e., wake, REM sleep, stages 1, 2, 3 or 4 of the NREM sleep, epoch with MT (movement time) annotation was not included in this work.

B. Preprocessing

The feature extraction phase is based on accurate QRS complex detection. For this reason we develop a new algorithm for R wave's locations using the multiscale wavelet analysis, based on singularity detection of local maxima of the wavelet coefficients [10].We used the QRS annotations to build the RR intervals, which defined as the interval from the peak of one QRS complex to the peak of the next.

C. Features extraction

In this paper, we extract the features from the RR intervals for sleep–wake stages scoring. The sleep stages are defined every 30-second. Then, for every epoch time of 30-second length, HRV features are extracted. This feature can be divided into two categories: time domain measures and frequency domain measures [11]. The time measures heart rate variability are defined in Table 1.Due to short epoch duration, only short term time-domain and frequency domain HRV features are used in this study [2].

Before the extraction of the frequency measures shown in TABLE 2, a preprocessing was carried out on the RR interval based on the fact that the spectral analysis cannot be affected only on regularly sampled signals [3]. This preprocessing is presented by resampling the data at a frequency of 1 Hz using an interpolation method developed by Berger et al [12].

Thus, the frequency measures were extracted from the power spectral density of the RR series by the Autoregressive Model (AR). The AR has fine properties to deal with non-stationary time series [7]. For this reason, the RR series is modeled by the autoregressive model (AR) which is presented as follows:

$$x = \sum_{i=1}^{p} ap(i)x(n-i) + e(n) \qquad (1)$$

Where p is the filter order, $x(n)$ is the sample n of RR intervals, $(a_i)_{i=1\ldots p}$ are the coefficients of the model, x denotes the prediction output. $e(n)$ is the prediction error, which present a white noise which has variance σ^2.
The estimation of coefficient of the AR model was determined by the Levinson-Durbin algorithm of order 13. The selection of this order can be verified by "arfit toolbox" [14], [13]. This selection is a compromise, because the proper order may vary. This is caused by short interval length and by the natural diversity in heart rates [14].

The coefficients $(a_i)_{i=1\ldots p}$ are used to estimate the power spectral density $P_{ar}(f)$ of the RR intervals, according to the following expression:

$$P_{ar}(f) = \frac{\sigma^2}{\left|1 - \sum_{i=1}^{p} ap(i)e^{-j2\pi fi}\right|^2} \qquad (2)$$

TABLE 1.Time-domain features

Features	Description
RRmean	Average of all RR intervals
SDNN	Standard deviation of all RR intervals
RMSSD	Square root of the mean of the squares of differences between adjacent RR intervals

TABLE 2. Frequency-domain features

Features	Description
TOTPWR	Total spectral power of all RR intervals up to 0.04 Hz
VLF	Total spectral power of all RR intervals between 0.003 and 0.04 Hz
LF	Total spectral power of all RR intervals between 0.04 and 0.15 Hz.
HF	Total spectral power of all RR intervals between 0.15 and 0.4 Hz
LF/HF	Ratio of low to high frequency power
LFnu	LF power in normalized units
HFnu	HF power in normalized units

D. ELM Classification

The classification is performed using a recent neural network algorithm: the Extreme Learning Machine (ELM). The ELM is known to achieve good performance in complex problems as well as reduce the computation time compared with other machine learning algorithms [15]. The information on this kind of neural network propagates directly from the input to output neurons through the hidden neurons. The architecture of this network organized in an input layer consisting of units representing the number of the extracted characteristic of the RR series, an output layer consisting on units representing the number of class and only one hidden layer. The connections in this architecture are established between neurons belong to successive layers and not between neurons in the same layer.

The ELM with a single hidden layer can be summarized as follows [16]:

Given a training set:

$\phi = \{(x_i, t_i)/x_i \in R^n, t_i \in R^m, i = 1, \dots, N\}$

Where x_i is a training sample and t_i is the corresponding target value, the activation function $g(x)$ and the number of hidden neurons$\tilde{N}$, perform the following steps.

Step1: Assign arbitrary input weight w_{ji} and bias b_i , $j = 1, \dots, \tilde{N}$

Step2: Calculate the output matrix at the hidden layer

$$H = g(w.x + b) \tag{3}$$

Step 3: Calculate the output weight β

$$\beta = H^{\dagger}T \tag{4}$$

Where $T = \begin{bmatrix} t_1^T \\ \\ \\ t_N^T \end{bmatrix}$

$H^{\dagger}$ is the Moore-Penrose generalized inverse of the matrix H

III. Experimental Results

All signals in the database MIT/BIH Polysomnographic were used to test the classification approach. First of all, we use the signals without deleted the epoch which carries the anomalies of apnea. Second, all epochs that carry these anomalies are eliminated. The automatic classification method proposed in this paper gives a label for each 30-second epoch. The two labels are Wake and Sleep as shown in Table 1, where: Wake (W) is a period when no sleep stages can be classified. Sleep (S) period includes sleep stage 1 or 2 or 3 or 4 or REM. The classification of these two classes of sleep was carried out by the ELM, classifier by fixing the number of input neurons to 10, which the corresponding number of features extracted. The output is set at the number of classes that is equal to 2 to classify 'W / S'. The number of hidden neurons is set at 300 after a study of several configurations, this is the learning process. The activation function chosen is the sigmoid function.

In this paper, the classification was performed with two scenarios: subject- specific system and subject-independent system. First a subject specific classification is trained by selecting epochs from 2/3 of the night's sleep with suitable representation of the two defined classes. Features were extracted from each epoch, and a classifier model was trained to distinguish the two classes, remaining 1/3 of the night's sleep was used to test the system [8]. Secondly, a subject-independent classification was constructed using training epochs drawn from all subjects. For this reason, we construct the training set by 2/3 of the database and 1/3 for testing.

In order to obtain quantitative results, it was computed the percentages of success results for each patient, which is the average of measurements repeated 6 times for each record. These results are shown in Fig. 2 and Fig. 3. In TABLE. 4 and TABLE. 5, we present the results of independent and specific classification. We note from these results that the rate of classification is different from wake to sleep class. In the sleep class and in case we have removed all epochs of 30 seconds which are individualized by anomalies of apnea, A subject specific classifier was trained and tested, and yielded an estimated classification accuracy of 83.59 %.When a subject-dependent classifier was trained and tested, the estimated classification accuracy dropped to 65.22 % . In the WAKE class, classification rate is always less than a sleep class. But, we can conclude that this classification rate is better when we used signals without apnea. The performance of the classifier on the subject independent task was poor, compared to specific classification.

By comparing the results obtained in this paper, we note that the classification rate is better than the results obtained by [9] when we have removed all epochs containing anomalies of apnea. in fact, we achieved a recognition rate of 83.59 % in order to classify the sleep class with time domain measures and frequency domain measures, and [6] obtained the classification rate is about 78.05% with HRV features, DFA features and PDFA features. It proves that our results are satisfactory compared to the number of feature parameters used when we remove the epoch of anomalies. Since a epoch with or without apnea does not have the same characteristic therefore it can influence the rate classification.

TABLE 3. Training and testing data in records of the MIT-BIH polysomnographic Database

	Epochs with anomalies of apnea		Epochs without anomalies of apnea	
	Wake	Sleep	Wake	Sleep
Training Data	1937	4736	1692	3110
Testing Data	968	2368	846	1554

TABLE 4.Results for subject-specific system

	Classification rate(with anomalies of apnea)		Classification rate(without anomalies of apnea)	
	Test	Train	Test	Train
Wake(W)	56.78	90.91	64.49	92.11
Sleep(S)	79.26	91.17	83.59	93.33

TABLE 5.Results for subject- independent system

	Classification rate(with anomalies of apnea)		Classification rate(without anomalies of apnea)	
	Test	Train	Test	Train
Wake(W)	40.59	80.53	51.65	89.25
Sleep(S)	59.34	81.47	65.22	90.03

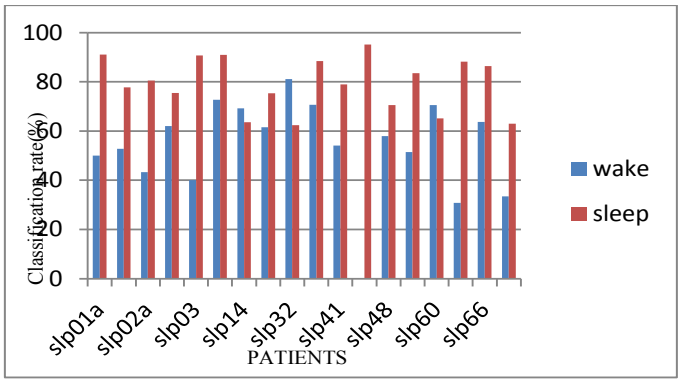

Figure 2. Percentages of successes results per patients (with anomalies of apnea).

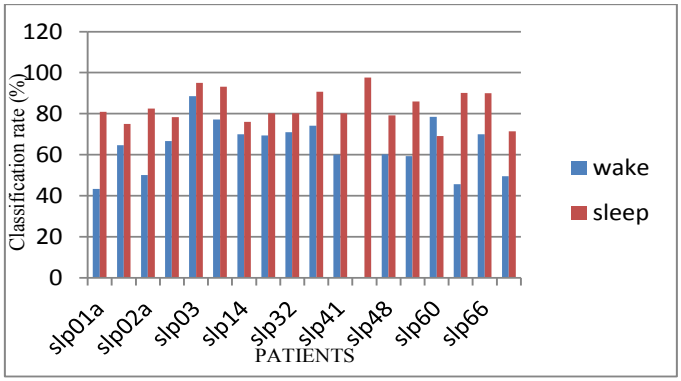

Figure 3. Percentages of successes results per patients (without anomalies of apnea).

IV. CONCLUSION

An automatic sleep-wake stages classifier based on signal ECG and using ELM tools was developed. The results show that good results can be obtained to classify sleep-wake stages when we use the method of HRV. In fact the HRV features were the markers of autonomic nervous system which changes during the stages of sleep. The results achieved are satisfactory for the classification of sleep stage and not satisfactory with wake stage classification.

We conclude that the ECG signal contains information related to sleep-wake stages, but we try in other works to separate the various stages in the sleep class (stage 1, stage 2, stage 3, stage 4 and REM stage).

REFERENCES

[1] D. Stéphanie, "Classification automatique en stades du sommeil : extraction de caractéristiques et comparaison des principaux classificateurs," Académie universitaire Wallonie- Bruxelles 2007.

[2] A. VIOLA, " La Variabilité Cardiaque au Cours des Cycles de Sommeil chez l'Homme," Thèse l'Université de STRASBOURG, 2004.

[3] M.Sami, M.Isa,Ito Wasito and Aniti Mur, "Kernel Dimensionality Reduction on Sleep Stage Classification using ECG Signal," IJCSI International Journal of Computer Science Issues, Vol. 8, Issue 4, No 2, July 2011.

[4] V.Vanoli, P.B Adamson, Ba-Lin, G.D. Pinna., R.Lazzara and Orr W.C, "Heart Rate Variability During Specific Sleep Stages Circulation," 91:pp.1918-1922, 1995.

[5] Malik M. , "Chairman of Writing Committee of Task Force of the European Society of Cardiology and the North American Society of Pacing Electrophysiology," Heart Rate Variability: Standards of Measurement, Physiological Interpretation, and Clinical Use, Circulation, 93:pp.1043-1065, 1996.

[6] M. Adnane and Z.Jiang , "Automatic sleep-wake stages classifier based on ECG ,"ICROS-SICE International Joint Conference 2009.

[7] M.O. Mendez, M. Matteucci, S. Cerutti, F. Aletti and A.M. Bianchi , "Sleep Staging Classification Based on HRV: Time-Variant Analysis ,"31st Annual International Conference of the IEEE EMBS Minneapolis, Minnesota, USA, September 2-6, 2009.

[8] S. Redmond and C Heneghan, "Electrocardiogram- BasedAutomatic Sleep Staging in Sleep Disordered Breathing", Computers in Cardiology 30:pp.609-612,2003.

[9] A. Goldberger, L. Amaral, L. Glass, J.M. Hausdorff, P.Ch. Ivanov, R.G. Mark, J.E. Mietus, G.B. Moody, C-K. Peng and H.E. Stanley, "PhysioBank, PhysioToolkit, and PhysioNet: Components of a New Research Resource for Complex Physiologic Signals", Circulation, Vol. 101, No. 23, pp. 215–220, 2000.

[10] H.Werteni, S.Yacoub and N. Ellouze, "Multiscale products for the detection of an electrocardiogramme R wave :MIT-BIH polysomnographic, " 6th International Conference: Sciences of Electronic Technologies of Information and Telecommunications 2012 .

[11] American Academy of Sleep Medicine Task Force, "Sleep-related breathing disorders in adults: Recommendations for syndrome definition and measurement techniques in clinical research Sleep," vol.22,pp.667–689,1999.

[12] RD. Berger,S. Akselrod and D. Gordon ,"An efficient algorithm for spectral analysis of the heart rate variability," IEEE Trans Biomed Eng., vol.33,pp. 220-222, 1986.

[13] T. Schneider and A. Neumaier ,"Algorithm. arfit—a matlab package for the estimation of parameters and eigenmodes of multivariate autoregressive models,"ACM Transactions on Mathematical Software, vol.27,pp.58–65.

[14] T.Al-ani, R.Kazbunda and D. Nov´ak ,"Automatic sleep scoring based only on electrocardiogram records ," ISBN 978-3-901608-32-2. Proc. EUROSIM 2007.

[15] G.-B. Huang, Q.-Y. Zhu and C.-K. Siew, "Extreme learning machine: Theory and applications," Neurocomputing, vol. 70, pp. 489-501, 2006.

[16] C.Kwak and O.Wook Kwon , "Cardiac Disorder Classification Based on Extreme Learning Machine," World Academy of Science, Engineering and Technology 48 2008.

Synchronization of the Liu chaotic system and its application in secure communication

Conference Paper · January 2017

DOI: 10.1109/CADIAG.2017.8075698

3 authors, including:

Souaia mohamed adnen Adnen
École Nationale d'Ingénieurs de Tunis
1 PUBLICATION **4** CITATIONS
SEE PROFILE

Kamel Ben Saad
École Nationale d'Ingénieurs de Tunis
62 PUBLICATIONS **289** CITATIONS
SEE PROFILE

Synchronization of the Liu chaotic system and its application in secure communication

Mohamed Adnen Souaia, Hatem Trabelsi, Kamel Ben Saad
Laboratoire de Recherche en Automatique (LA.R.A), ENIT
Tunis Belvédère, Tunisia
mohamedadnens@gmail.com, 7atem.trabelsi@gmail.com, kamel.bensaad@enit.rnu.tn

***Abstract*—This paper addresses the chaos synchronization of two identical drive-response Liu chaotic systems and its application in secure communication. Based on the vector norm approach, a control law is developed and applied to synchronize both systems' states. The obtained synchronization scheme is implemented using analog circuits and applied for chaos masking communication. Simulation results are presented to demonstrate the effectiveness of the proposed communication system.**

Keywords—Liu chaotic system; synchronization; vector norms; Borne and Gentina stability criterion; secured communication;

I. Introduction

Chaos is a complex dynamical phenomenon characterizing several nonlinear systems. Chaotic behavior, which occurs in many natural processes, is associated with unpredictability and sensitive dependence to initial conditions. The study of chaos has become a popular field of research since Pecora and Carroll introduced the synchronization of chaotic systems in 1990 [1]. Various applications of chaos synchronization have been investigated, including biological systems [2], chemical reactions [3], physical systems [4], secure communication [5-6] etc. Among many concepts of chaos synchronization, the most common one is the drive-response configuration. This means that two chaotic systems are coupled in such a way that the trajectories of the response system converge, in finite time, to those of the drive system. Different synchronization approaches have been proposed, such as nonlinear control [7], nonlinear observer [8], fuzzy control [9], backstepping control [10], vector norms [11-12], etc.

In this paper, we investigate the synchronization of the Liu chaotic system [13] and its application for secure communication. The vector norms approach is adopted for the development of a synchronizing control law. We use the practical Borne and Gentina stability criterion [14] associated with the Benrejeb arrow form description [15-16] for the system state matrix. The developed synchronization scheme is then applied for a secure communication system and implemented using analog electronic devices.

The paper is organized as follows. Section 2 addresses the synchronization of the Liu chaotic system using the vector norms approach. Section 3 presents a Liu based secured chaotic communication scheme and its implementation. Simulation results are presented in Section 4 to finish with some concluding remarks in Section 5.

II. Synchronization of the Liu chaotic system

A. The chaotic Liu system

In 2004, Liu et al. proposed a three-dimensional chaotic system with only two quadratic terms [13]. The Liu chaotic system can be described by the following differential equation:

$$\begin{cases} \dot{x} = a(y - x) \\ \dot{y} = bx - kxz \\ \dot{z} = -cz + hx^2 \end{cases} \quad (1)$$

where x, y and z are system states and a, b, c, h and k are positive parameters. For a=10, b=40, c=2.5, h=4 and k=1 system (1) exhibits a chaotic attractor as shown in figure 1. The Liu system has three equilibrium points:

$$O(0,0,0)\ ,\ E_1(x_0, y_0, z_0) \ \text{ and } \ E_2(-x_0, -y_0, z_0)$$

where $x_0 = y_0 = \sqrt{bc/(hk)}$ and $z_0 = b/k$.

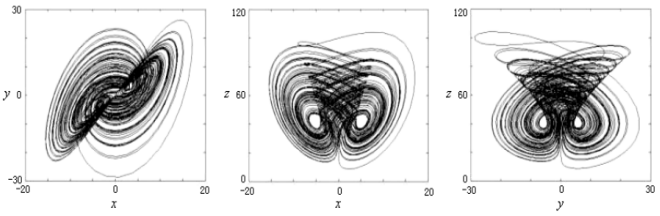

Fig. 1. Projections of the Liu chaotic attractor

B. Problem statement

Consider a chaotic Liu drive system described by:

$$\begin{cases} \dot{x}_1 = a(x_2 - x_1) \\ \dot{x}_2 = bx_1 - kx_1x_3 \\ \dot{x}_3 = -cx_3 + hx_1^2 \end{cases} \quad (2)$$

The controlled Liu response system is expressed by:

$$\begin{cases} \dot{y}_1 = a(y_2 - y_1) + u_1 \\ \dot{y}_2 = by_1 - ky_1y_3 + u_2 \\ \dot{y}_3 = -cy_3 + hy_1^2 + u_3 \end{cases} \quad (3)$$

where u_1, u_2 and u_3 are the control signals.

Define the synchronization error as

$$e = (e_1, e_2, e_3)^t \triangleq (x_1 - y_1, x_2 - y_2, x_3 - y_3)^t \quad (4)$$

Then, the error dynamical system is obtained as follows:

$$\begin{cases} \dot{e}_1 = a(x_2 - x_1) - a(y_2 - y_1) - u_1 \\ \dot{e}_2 = bx_1 - kx_1x_3 - by_1 + ky_1y_3 - u_2 \\ \dot{e}_3 = -cx_3 + hx_1^2 + cy_3 - hy_1^2 - u_3 \end{cases} \quad (5)$$

and can be expressed in terms of the synchronization error states by

$$\begin{cases} \dot{e}_1 = a(e_2 - e_1) - u_1 \\ \dot{e}_2 = be_1 - kx_3e_1 - ky_1e_3 - u_2 \\ \dot{e}_3 = -ce_3 + h(x_1 + y_1)e_1 - u_3 \end{cases} \quad (6)$$

Using a state feedback control law as:

$$u_i = -\sum_{j=1}^{3} k_{ij}e_j \text{ , } i=1,\ldots,3. \quad (7)$$

an equivalent matrix representation of system (6) is the following:

$$\dot{e} = A(.)e \quad (8)$$

with

$$A(.) = \begin{pmatrix} -a + k_{11} & a + k_{12} & k_{13} \\ b - kx_3 + k_{21} & k_{22} & -ky_1 + k_{23} \\ h(x_1 + y_1) + k_{31} & k_{32} & -c + k_{33} \end{pmatrix} \quad (9)$$

Systems (2) and (3) are said to be synchronized if

$$\lim_{t \to \infty} \|e(t)\| = 0 \text{ for all } e(0) \in \mathbb{R}^3. \quad (10)$$

In other words, the synchronization between the two coupled chaotic Liu systems (2) and (3) can be achieved if the error dynamical system described by (8) is stable. Thus, the main objective here is to design a control law according to (7) ensuring the stability of t system (8).

C. *Vector norms based synchronization of the Liu chaotic system*

In this subsection, we use the vector norm approach to develop a synchronizing control law for systems (3). As mentioned, this issue is equivalent to a stabilization problem of the error dynamical system (8) which can be solved according to the Borne and Gentina practical stability criterion (See Appendix).

Theorem 1: The synchronization between coupled Liu chaotic systems (2) and (3) is achieved when the following control law is applied:

$$\begin{cases} u_1 = 0 \\ u_2 = x_1(b - kx_3 + \varepsilon) - y_1(b - ky_3 + \varepsilon) \\ u_3 = 0 \end{cases} \quad (11)$$

where $0 < \varepsilon < \frac{1}{2}a$.

Proof :

Consider the linear transformation given by:

$$F(.) = P^{-1}A(.)P \quad (12)$$

where

$$P = \begin{pmatrix} 0 & 0 & -2 \\ 0 & -1 & -1 \\ 1 & 0 & 0 \end{pmatrix} \quad (13)$$

Applying this transformation to the characteristic matrix of system (8) yields a new matrix *F(.)* with the same spectrum as *A(.)*. If the gain k_{23} is choose as

$$k_{23} = ky_1 \quad (14)$$

and all the state feedback gains are fixed to zero excepting k_{21}, the new characteristic matrix *F(.)* has the following arrow form:

$$F(.) = \begin{pmatrix} -c & 0 & -2h(x_1 + y_1) \\ 0 & -\frac{1}{2}a & \frac{1}{2}a + 2b - 2kx_3 + 2k_{21} \\ 0 & \frac{1}{2}a & -\frac{1}{2}a \end{pmatrix} \quad (15)$$

The use of the vector norm defined by:

$$|x| = (|x_1|, |x_2|, \ldots, |x_n|) \quad (16)$$

leads to an overvaluing matrix $\bar{F}(.)$ for the system characterized by *F(.)*, in which all the non constant elements are isolated in one column:

$$\bar{F}(.) = \begin{pmatrix} -c & 0 & |2h(x_1 + y_1)| \\ 0 & -\frac{1}{2}a & \left|\frac{1}{2}a + 2b - 2kx_3 + 2k_{21}\right| \\ 0 & \left|\frac{1}{2}a\right| & -\frac{1}{2}a \end{pmatrix} \quad (17)$$

The application of the practical Borne and Gentina stability criterion to the matrix *F(.)* allows to conclude that the system characterized by *F(.)* and consequently system (8) is stable if

$$\det(\bar{F}(.)) = -c\left(\frac{a^2}{4} - \frac{1}{2}\left|\frac{1}{2}a + 2b - 2kx_3 + 2k_{21}\right||a|\right) < 0 \quad (18)$$

Given the sign of the parameter *a*, (18) is equivalent to

$$\left|\frac{1}{2}a + 2b - 2kx_3 + 2k_{21}\right| < \frac{1}{2}a \quad (19)$$

and has as solution:

$$-b + kx_3 - \frac{1}{2}a < k_{21} < -b + kx_3 \quad (20)$$

Then, a possible choice for the state feedback gain k_{21} is the following:

$$k_{21} = -b + kx_3 - \varepsilon \text{ , } 0 < \varepsilon < \frac{1}{2}a \quad (21)$$

Finally, by substituting (14) and (21) into (7) we find the control law expression in theorem 1.

III. Secure communication using the chaotic Liu system

A. The chaotic masking scheme

Because of their rich dynamics and their noise-like behavior difficult to predict, chaotic signals have been widely used in communication applications for masking information. A very common communication scheme using chaos is the chaotic masking.

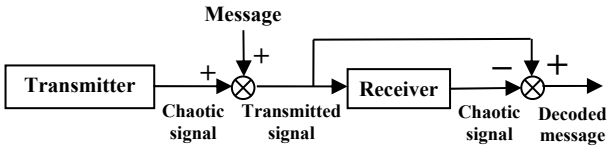

Fig. 2. The chaotic masking technique scheme

A chaotic signal is added to the message at the transmitter, as illustrated by figure 1, then regenerated and subtracted by the receiver [17, 18, 19].

B. Circuit realization of the drive and response systems

The circuitry realizing equation (1) governing the Liu chaotic system dynamics is presented in fig. 3. (the drive system) and fig. 4. (the response system).

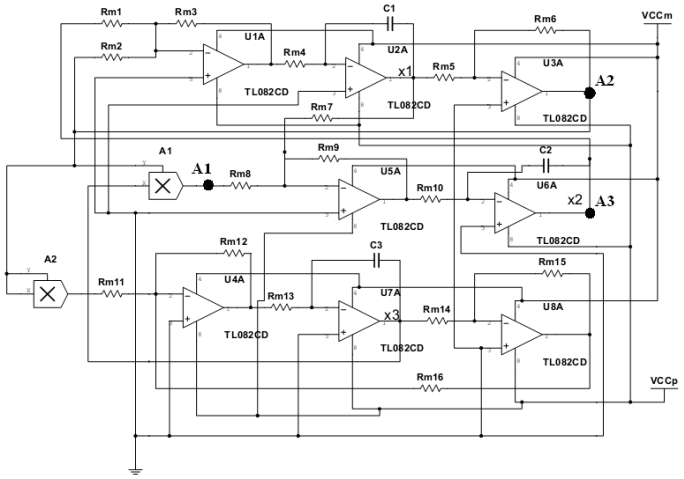

Fig. 3. Realization of the master Liu chaotic system

Chaotic circuits are built using operational amplifier circuits to realize mathematical operations like summation, multiplication and integration. The TL082 is used as operational amplifier and the AD633 as analog multiplier. Other passive components have the same following values in both circuits:

$C_1 = C_2 = C_3 = 1\mu F$, $R_{m1} = 10k\Omega$, $R_{m2} = 20k\Omega$, $R_{m3} = 10k\Omega$, $R_{m4} = 100k\Omega$, $R_{m5} = 10k\Omega$, $R_{m6} = 20k\Omega$, $R_{m7} = 10k\Omega$, $R_{m8} = 80k\Omega$, $R_{m9} = 40k\Omega$, $R_{m10} = 100k\Omega$, $R_{m11} = 10k\Omega$, $R_{m12} = 10k\Omega$, $R_{m13} = 100k\Omega$, $R_{m14} = 10k\Omega$, $R_{m15} = 10k\Omega$ and $R_{m16} = 40k\Omega$.

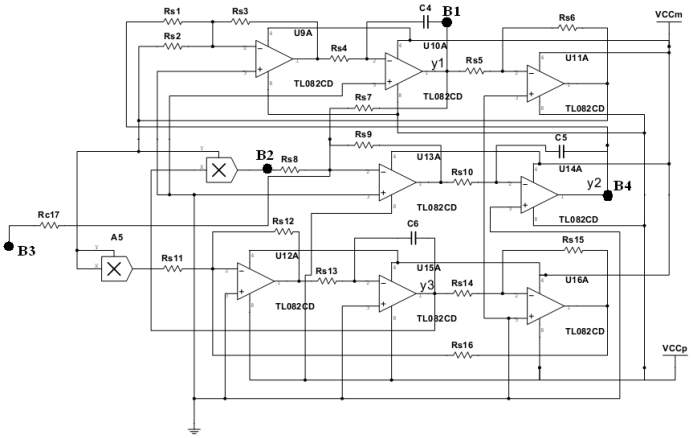

Fig. 4. Realization of the slave Liu chaotic system

The power supply is $\pm 15V$ and the control signal used for synchronization is injected to the response system through the resistor $R_{c17} = 100\,k\Omega$ in the analog adder entry.

C. Implementation of the control law and the masking system

The control law (11) is realized as illustrated by fig. 5.

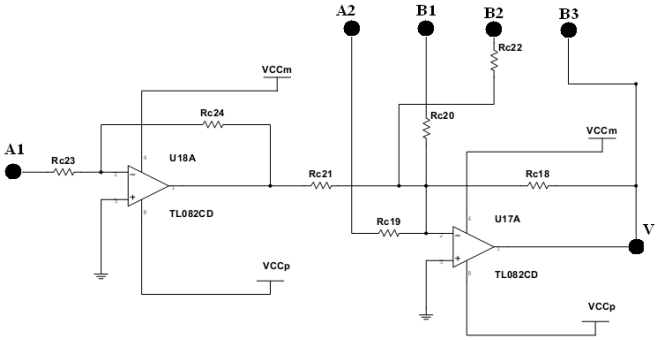

Fig. 5. Implementation of the control law

The used resistors have the following resistances: $R_{c18} = 210\,k\Omega$, $R_{c19} = 40\,k\Omega$, $R_{c20} = 20\,k\Omega$, $R_{c21} = 169\,k\Omega$, $R_{c22} = 169\,k\Omega$, $R_{c23} = 100\,k\Omega$ and $R_{c24} = 100\,k\Omega$.

Finally, the masking circuit which is made by cascaded analog adders is represented by fig. 6. The resistances used are:

$R_1 = ... = R_6 = 100\,k\Omega$

We should mention here that the developed control law, beside its effectiveness, has many practical advantages making it more suitable for implementation than other synchronization schemes proposed in literature [20, 21, 22]. In fact, only one controller is needed and only one signal is needed to be transmitted from the drive system to the controller.

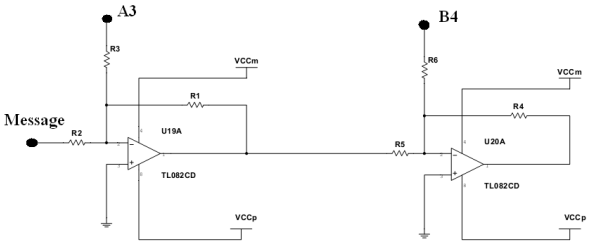

Fig. 6. The masking system

IV. Simulation results

In order to validate the proposed synchronizing law (11), Matlab simulations have been carried out. Using the fourth-order Runge-Kutta method with a time step size of 0.001 s, the time evolution of the synchronization errors has been simulated before and after the application of the control law, as shown, respectively, in figure 1 and figure 2.

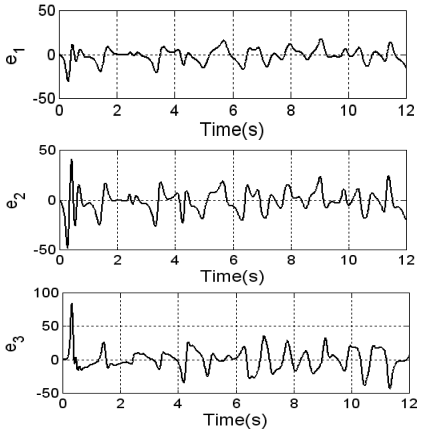

Fig. 7. Synchronization errors when control is disabled

The considered value of the parameter ε is (1/2.2) and initial conditions are fixed as : $(x_{10}, x_{30}, x_{30}) = (0.1,\ 0.2,\ 0.1)$ for the master system and $(y_{10}, y_{30}, y_{30}) = (-0.5, -0.4,\ 0.5)$ for the slave one. Simulation results demonstrate that synchronization has been achieved in less than 1 second and with a tolerable overshoot which can be reduced using another value for the parameter ε .

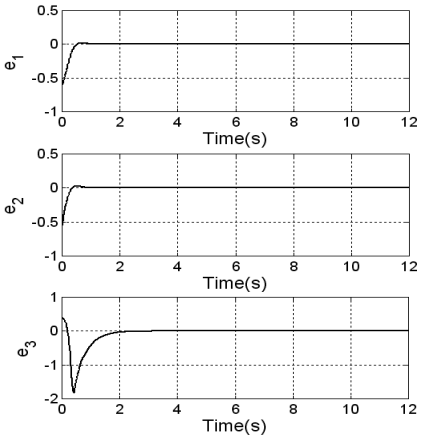

Fig. 8. Synchronization errors when control is activated

The secure communication system, as implemented by analog circuits, has been simulated using the NI Multisim 12.0 software. The transmitted message is a sinusoidal signal of 1Hz frequency and 2V amplitude. As shown in fig.1, the transmitted message has been decoded correctly.

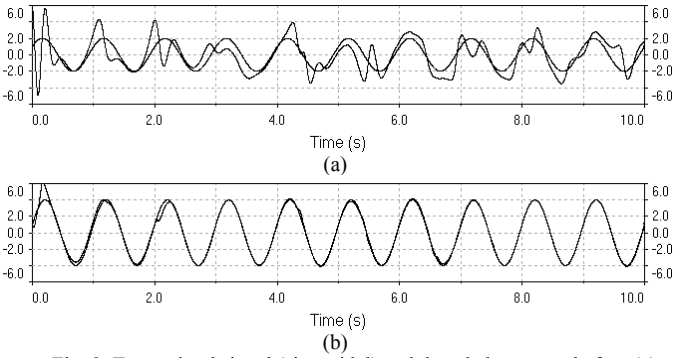

Fig. 9. Transmitted signal (sinusoidal) and decoded message before (a) and after (b) the application of the control law

The chaotic signal used for masking is the x_2 state generated by the master chaotic system. Similar results have been obtained for different kinds of signals transmitted as messages.

V. Conclusion

This paper investigates the synchronization of the chaotic Liu systems using a vector norms based approach. A synchronizing control law is developed using the practical Borne and Gentina stability criterion associated with the Benrejeb arrow form matrix description for the error dynamical system. The obtained synchronization scheme is then applied and implemented in a secure communication system. The effectiveness of the proposed results is illustrated by the means of numerical simulations.

Appendix

Kotelyanski lemma [14]

The real parts of the eigenvalues of a matrix A, with non negative off diagonal elements, are less than a real number μ if and only if all those of matrix $M = \mu I_n - A$ are positive, with I_n the n identity matrix.

If the successive principal minors of matrix $(-A)$ are positive, Kotelyanski lemma permits to conclude on stability property of the system characterized by A .

Borne and Gentina practical stability criterion [14]

Consider a nonlinear continuous process described by the following state space representation:

$$\dot{x} = A(.)x \quad (x \in \mathbb{R}^n,\ A(.) \in \mathbb{R}^{n \times n})$$

and let $M(A(.))$ denotes the overvaluing matrix of the system $\dot{x} = A(.)x$, with respect to a vector norm $p(x)$, defined

by the inequality:

$$\dot{p}(x) \le M(A(.))p(x)$$

which must be fulfilled for each corresponding component.

If the overvaluing matrix has its non constant elements isolated in only one row, the verification of the Kotelyanski lemma allows to conclude about the stability of the initial system.

For example, if the non constant elements are isolated in only one row of $A(.)$, the application of the Kotelyanski lemma to the overvaluing matrix obtained by the use of the vector norm:

$$p(x) = (|x_1|,...,|x_n|)^t$$

implies the following stability conditions for the initial system described by $A(.)$:

$$a_{11} < 0 \ , \begin{vmatrix} a_{11} & |a_{12}| \\ |a_{21}| & a_{22} \end{vmatrix} > 0 \ , \dots , \ (-1)^n \begin{vmatrix} a_{11} & |a_{12}| & \cdots & |a_{1n}| \\ |a_{21}| & a_{22} & \cdots & |a_{2n}| \\ \vdots & \vdots & \ddots & \vdots \\ |a_{n1}| & |a_{n2}| & \cdots & a_{nn} \end{vmatrix} > 0$$

In the particular case where the characteristic matrix $A(.)$ is in arrow form, also called the Benrejeb form [16], with negative diagonal entries, the above stability conditions are reduced to:

$$(-1)^n (a_{nn} - \sum_{i=1}^{n-1} |a_{ni} a_{in}| a_{ii}^{-1}) > 0$$

References

[1] [1] L. M. Pecora and T. L. Carroll. Synchronization in chaotic systems. Phys. Rev. Lett. 64, pp. 821–824, 1990.

[2] [2] R.A. Ims, H.P. Andreassen. Spatial synchronization of vole population dynamics by predatory birds, Nature, vol. 408, pp. 194-196, 2000.

[3] [3] Y.N. Li, L. Chen, Z.S. Cai, X.Z. Zhao. Experimental study of chaos synchronization in the Belousov-Zhabotinsky chemical system, Chaos Solitons Fractals, vol. 22, no. 4, 767-771, 2004.

[4] [4] M. Lakshmanan and K. Murali, Chaos in Nonlinear Oscillators: Controlling and Synchronization, World Scientific, Singapore, 1996.

[5] [5] K.M. Cuomo and A.V. Oppenheim, "Circuit implementation of synchronized chaos with application to communication", Phys. Rev. Lett., vol. 71, pp. 65-68, 1993.

[6] L. Kacarev, U. Parlitz: General approach for chaotic synchronization, with application to communication, Physical Review Letters, vol. 74, 5028-5031, 1996.

[7] Elabbasy E., Agiza H., El-Dessoky M.: Global chaos synchronization for four scroll attractor by nonlinear control, Sci. Res. Essay 1 pp. 65–71, 2006.

[8] Nijmeijer H. and Mareels I.M.Y.: An observer looks at synchronization, IEEE Trans. Cicuits Syst. I (44), pp. 882–890, 1997.

[9] Yau H.T. and Shieh C.S.: Chaos synchronization using fuzzy logic controller, Nonlinear Analysis: Real World Applications, 2007.

[10] Tan X., Zhang J. and Yang Y.: Synchronizing chaotic systems using backstepping design, Chaos, Solitons & Fractals, 16, pp. 37–45, 2003.

[11] S. Hammami, K. Ben saad, and M. Benrejeb, "On the synchronization of identical and non-dentical 4-D chaotic systems using arrow form matrix", Chaos, Solitons and Fractals, 42, pp. 101–112, 2009.

[12] Trabelsi H. and Benrejeb M. Combination synchronization of hyperchaotic complex systems a vector norm based approach. 7th International Conference on Modelling, Identification and Control (ICMIC), Sousse, Tunisia, 2015.

[13] C. Liu, T. Liu, L. Liu, K. Liu, "A new chaotic attractor", Chaos Solitons Fractals 22, pp. 1031–1038, 2004.

[14] J.C. Gentina, P. Borne and F. Laurent, "Stabilité des systèmes continus non linéaires de grande dimension ", RAIRO, Août, J-3, pp. 69-77, 1972.

[15] Benrejeb M. On the Use of Arrow Form Matrices for Processes Stability and Stabilizability Studies. 2nd International Conference on Systems and Computer Science (ICSCS) Villeneuve d'Ascq, France, August 26-27, 2013.

[16] P. Borne. P. Vanheeghe, E. Duflos. Automatisation des processus dans l'espace d'état. Ed. Technip, Paris, 2007.

[17] K. M. Cuomo, A. V. Oppenheim, and S. H. Isabelle, "Spread spectrum modulation and signal masking using synchronized chaotic systems", Research Laboratory of Electronics, Massachusetts Institute of Technology, Cambridge, TR 570, 1992.

[18] A. V. Oppenheim, G. W. Womell, S. H. Isabelle, and K. M. Cuomo, "Signal processing in the context of chaotic signals", Proc.

[19] K. M. Cuomo and A. V. Oppenheim, "*Chaotic signals and systems for communications*," in Proceedings of 1993 IEEE ICASSP HI, pp. 137-140, 1993.

[20] V. Sundarapandian, "Global Chaos Anti-Synchronization of Liu and Chen Systems by Nonlinear Control", International Journal of Mathematical Sciences and Applications Vol. 1 No. 2, May, 2011.

[21] V. Sundarapandian, "Hybrid synchronizaion of Liu and Lü chaotic systems via adaptive control", International Journal of Advanced Information Technology (IJAIT) Vol. 1, No. 6, December, 2011.

[22] Y. Chen, Z. Jia, "Parameters identification and projective dislocated lag synchronization of Liu chaotic system via adaptive control", IJRRAS 12 (1), July 2012.

Arab J Sci Eng
DOI 10.1007/s13369-016-2196-1

RESEARCH ARTICLE - MECHANICAL ENGINEERING

Application of the Independent Components Analysis in the Reconstruction of Acoustic Sources in Duct Systems

Raja Dhief[1] · Mohamed Taktak[1,2] · Dhouha Tounsi[2] · Ali Akrout[2] · Mohamed Haddar[2]

Received: 3 July 2015 / Accepted: 11 May 2016

Abstract The development of new reconstruction methods of acoustic sources presents a domain of great interest seen its applications in reducing the noise, realizing the acoustic comfort and diagnosing systems. The duct systems are used in several systems such as building, ventilation and aeronautic systems. In this work, a new reconstruction technique of the acoustic sources in duct systems is presented. This technique is based on the multimodal scattering matrix that provides an estimation of the acoustic power dissipation and attenuation in the case of a point acoustic source. These energetic parameters are then injected into an identification technique based on the independent component analysis technique allowing the reconstruction of original sources. The method was applied to a cylindrical rigid-lined-rigid duct element. A comparison between the estimated and imposed acoustic pressures emitted by point sources is presented. This comparison showed that the proposed method gives good results, and the original signals are well reconstructed.

Keywords Inverse method · ICA (independent components analysis) · Reconstruction · Acoustics source · Duct systems

1 Introduction

The reconstruction of acoustic sources is a promising technique for the study of physical systems. Acoustic sources reconstruction methods belong to the most widely known inverse problems. They consist on the determination of the acoustic sources in systems from measurements of acoustic quantities (pressure, sound velocity, etc.). These sources can be physical sources of noise (speaker, fan, etc.) or produced by defects in the studied system.

The use of these techniques is justified by the fact that the systems cannot be instrumented by sensitive sensors to isolate the acoustic waves generated from specific sources. The source reconstruction techniques are widely used in the aerospace, building and automotive industries to improve techniques of reducing noise sources in order to meet current regulations and increase the acoustic comfort. Many works were carried on the field of reconstruction of acoustic sources in duct systems mostly used in these industries. Hewlett and Nelson [1] presented a method based on an inverse technique coupling between an analytical model and the experiment to reconstruct the sound source strength in duct systems. Nelson and Yoon [2,3] presented also a model based on an inverse method for source reconstruction in duct systems based on the use of pressure and/or velocity measurements at discrete points over a virtual surface and an analytical acoustic propagation model inside the duct element between the sources and the measurement points. Kim and Nelson [4–6] presented a coupled experimental and analytical method for deducing the strength of an acoustic source distribution from measurements of the internal field in a semi-infinite duct element with an open end. They used the singular value decomposition (SVD) to inverse the matrix of frequency response relating measurements and sources. Schumacher et al. [7] used numerical method called the inverse boundary element method (IBEM) to resolve this problem. Bravo and Maury [8,9] developed an analytical model for the acoustic source reconstruction in ducts using the equivalent source method (ESM). This technique shows limitations in the source distribution assumption. To surpass these limitations, Bravo and

✉ Mohamed Taktak
mohamed.taktak@fss.rnu.tn

[1] Faculty of Sciences of Sfax, BP No. 1171, 3000, Sfax, Tunisia

[2] Laboratory of Mechanics Modeling and Production (LA2MP), National School of Engineers of Sfax, University of Sfax, BP No. 1173, 3038, Sfax, Tunisia

Published online: 27 May 2016

Maury [10] used the beamforming techniques. Finally, They used the spectral decomposition method (SDM) based on decomposing the source strength as Fourier series coupled with a minimization of a mean square error criterion [11–13]. Recently, Zhong et al. [14] used the beamforming method to identify the sound source location in duct systems.

The independent component analysis (ICA) is one of the blind reconstruction techniques allowing recovering a finite set of unknown signals (sources) from a finite set of observed signals (measurements) which represents a combination of source signals without any knowledge about the sources and propagation medium. This technique is based on the decomposing of the measured signals into statistically independent components. This technique was used successfully in previous works to estimates sources in mechanical systems [15–18] and showed its efficiency to recover sources signals.

The aim of this work is to develop a technique of reconstruction of acoustic sources in duct systems. This method is based on the multimodal scattering matrix as well as the modal pressures generated by a point source attached to the duct wall. From these quantities, the modal acoustic power dissipations and attenuations are computed. These quantities are used as inputs of the independent component analysis technique to reconstruct acoustic pressures emitted by the corresponding sources. The outline of the paper is following: After having presented the studied problem in the Sect. 2, the theoretical basis about the multimodal scattering matrix, the modal pressures emitted from a point acoustic source and the computation of the acoustic power dissipation and attenuation are presented in Sect. 3. In Sect. 4, the independent component analysis method is presented. Finally and in Sect. 5, the results of the proposed reconstruction technique for two point sources are presented and discussed.

2 The Studied Duct Configuration

The studied duct is presented in Fig. 1: It is a cylindrical duct composed by:

- A source duct in which a point source is located at the cylindrical coordinates z_s and θ_s and characterized by its amplitude A_s and its phase φ_s.
- A 1 m long element duct located between z_R and z_L (The value of z_L is chosen as the reference value of the z axis) and composed of 3 parts: 0.35 m hard wall duct, 0.3 m lined wall duct and 0.35 m hard wall duct. The study is carried out with a liner modeled by a constant acoustic impedance Z in the lined part of the duct and equal to $1+i$.
- The end duct supposed nonreflective.

3 Theoretical Basis

3.1 Multimodal Scattering Matrix

The element duct located between z_L and z_R is characterized by its multimodal scattering matrix $\boldsymbol{S}_{2N\times 2N}$, with N is the number of propagating modes, relating the out coming pressure waves array $\boldsymbol{P}_{2N}^{\text{out}} = \left\langle P_{00}^{I-}, \ldots, P_{PQ}^{I-}, P_{00}^{II+}, \ldots, P_{PQ}^{II+} \right\rangle_N^T$ to incoming pressure waves array $\boldsymbol{P}_{2N}^{\text{in}} = \left\langle P_{00}^{I+}, \ldots, P_{PQ}^{I+}, P_{00}^{II-}, \ldots, P_{PQ}^{II-} \right\rangle_N^T$ (Fig. 1) [19]:

$$\boldsymbol{P}_{2N}^{\text{out}} = \boldsymbol{S}_{2N\times 2N}\boldsymbol{P}_{2N}^{\text{in}} = \begin{bmatrix} \boldsymbol{R}_{N\times N} & \boldsymbol{T}_{N\times N} \\ \boldsymbol{T}_{N\times N} & \boldsymbol{R}_{N\times N} \end{bmatrix}_{2N\times 2N} \boldsymbol{P}_{2N}^{\text{in}} \tag{1}$$

m and n are, respectively, the azimuthal and the radial mode numbers. P and Q are, respectively, angular and radial wave numbers associated with the Nth propagating mode ($m \leq P$ and $n \leq Q$). The use of the multimodal scattering matrix is justified by the fact that this matrix is an intrinsic characteristic of the duct independently of the upstream and downstream acoustic conditions of the element. This matrix is computed numerically as presented in a previous work [19].

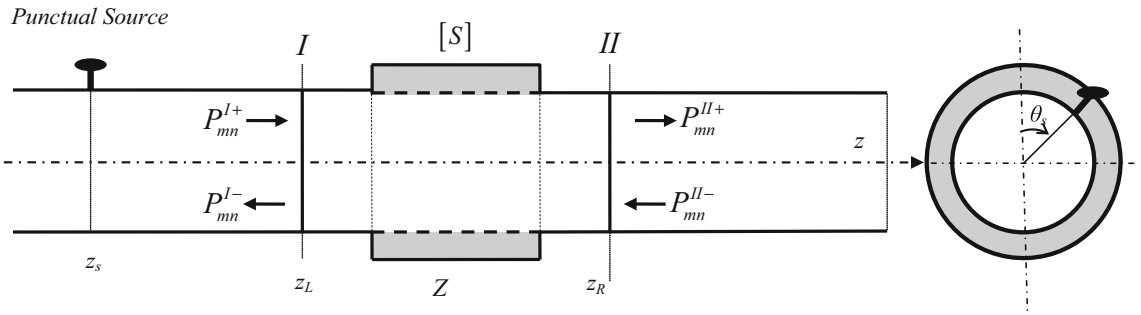

Fig. 1 Studied duct element configuration

3.2 Modal Acoustic Pressures Emitted from a Point Acoustic Source

In the present study, the point source, characterized, respectively, by the amplitude A_s and the phase φ_s, is mounted on the wall localized at θ_s and z_s (Fig. 1). The expression of the incident pressure at z_L associated with the mode (m, n) is given by Akoum et al. [20] and Sitel et al. [21] as follows:

$$P_{mn}^{I+} = A_s \cdot \alpha_{mn} e^{j(\varphi_s - m\theta_s + k_{mn}(z_L - z_s))} \tag{2}$$

$$\alpha_{mn} = \frac{1}{2jk_{mn}N_{mn}} \tag{3}$$

$$k_{mn} = \sqrt{k^2 - (\chi_{mn}/a)^2} \tag{4}$$

k_{mn} is the axial wave number associated with the mode (m, n) in the main duct, χ_{mn} is the nth root satisfying the radial hard wall boundary condition on the wall of the main duct, a is the duct radius. $k = 2\pi f/c_0$ with c_0 is the speed of sound in air and f is the spatial frequency. N_{mn} is the normalization factor associated with the (m, n) mode defined as follows [19–22] (see "Appendix"):

$$\begin{cases} N_{00} = 1 \\ N_{mn} = SJ_m^2(\chi_{mn})\left(1 - \frac{m^2}{\chi_{mn}^2}\right) \end{cases} \tag{5}$$

$S = \pi a^2$ is the cross-sectional area, and J_m is the Bessel function of the first kind of order m. In the case of N propagating modes, the vector of modal incident pressures emitted by the point source is given as follows:

$$\boldsymbol{P}_N^{I+} = \begin{Bmatrix} \vdots \\ P_{mn}^{I+}(z_L) \\ \vdots \\ P_{pq}^{I+}(z_L) \\ \vdots \end{Bmatrix}_N = \begin{Bmatrix} \vdots \\ A_s \cdot \alpha_{mn} e^{j(\varphi_s - m\theta_s + k_{mn}(z_L - z_s))} \\ \vdots \\ A_s \cdot \alpha_{pq} e^{j(\varphi_s - p\theta_s + k_{pq}(z_L - z_s))} \\ \vdots \end{Bmatrix}_N \tag{6}$$

3.3 Acoustic Power Dissipation and Attenuation

The acoustic dissipation and attenuation are energetic quantities allowing the evaluation of the efficiency of acoustic systems. The acoustic power at a section localized at z is given as follows [22]:

$$W(z) = \sum_{m=-\infty}^{+\infty} \sum_{n=0}^{\infty} I_{z,mn}(z) N_{mn} \tag{7}$$

$I_{z,mn}$ is the axial acoustic intensity associated with the (m, n) mode defined by:

$$I_{z,mn}(z) = \frac{1}{2} R_e \left(P_{mn}(z) \cdot V_{z,mn}^*(z) \right) \tag{8}$$

$V_{z,mn}^*(z)$ is the complex conjugate of the axial acoustic particle velocity.

The incident, reflected, transmitted and retrograde modal intensities are given by the following expressions:

$$\begin{aligned} I_{z,mn}^{I\pm}(z_L) &= \frac{N_{mn} \cdot k_{mn}}{2c_0\rho_0 k} \left| P_{mn}^{I\pm}(z_L) \right|^2; \\ I_{z,mn}^{II\pm}(z_R) &= \frac{N_{z,mn} \cdot k_{mn}}{2c_0\rho_0 k} \left| P_{mn}^{II\pm}(z_R) \right|^2 \end{aligned} \tag{9}$$

The acoustic power dissipation, W_{dis}, of a duct with two ports is the difference between the acoustic power of the incoming waves W^{in} and the acoustic power of outgoing waves W^{out}.

$$W_{\text{dis}} = W^{\text{in}} - W^{\text{out}} \tag{10}$$

$$W^{\text{in}} = \sum_{m=-P}^{P} \sum_{n=0}^{Q} \frac{N_{mn} \cdot k_{mn}}{2c_0\rho_0 k} \left(\left| P_{mn}^{I+}(z_L) \right|^2 + \left| P_{mn}^{II-}(z_R) \right|^2 \right);$$

$$W^{\text{out}} = \sum_{m=-P}^{P} \sum_{n=0}^{Q} \frac{N_{mn} \cdot k_{mn}}{2c_0\rho_0 k} \left(\left| P_{mn}^{I-}(z_L) \right|^2 + \left| P_{mn}^{II+}(z_R) \right|^2 \right) \tag{11}$$

The acoustic power dissipation W_{dis} is deduced from the scattering matrix. Indeed, the acoustic powers (11) can be written on the following forms:

$$W^{\text{in}} = \boldsymbol{\Pi}_{2N}^{\text{in}\,T^*} \cdot \boldsymbol{\Pi}_{2N}^{\text{in}}; \quad W^{\text{out}} = \boldsymbol{\Pi}_{2N}^{\text{out}\,T^*} \cdot \boldsymbol{\Pi}_{2N}^{\text{out}} \tag{12}$$

$$\boldsymbol{\Pi}_{2N}^{\text{in}} = \left\langle \Pi_{00}^{I+}(z_L), \ldots, \Pi_{PQ}^{I+}(z_L), \Pi_{00}^{II-}(z_R), \ldots, \Pi_{PQ}^{II-}(z_R) \right\rangle \tag{13}$$

$$\boldsymbol{\Pi}_{2N}^{\text{out}} = \left\langle \Pi_{00}^{I-}(z_L), \ldots, \Pi_{PQ}^{I-}(z_L), \Pi_{00}^{II+}(z_R), \ldots, \Pi_{PQ}^{II+}(z_R) \right\rangle \tag{14}$$

The following matrix relation is deduced:

$$\begin{aligned} \boldsymbol{\Pi}_{2N}^{\text{out}} &= \boldsymbol{S}'_{2N\times 2N} \cdot \boldsymbol{\Pi}_{2N}^{\text{in}} \\ &= \boldsymbol{X}_{2N\times 2N} \cdot \boldsymbol{S}_{2N\times 2N} \cdot \boldsymbol{X}_{2N\times 2N}^{-1} \cdot \boldsymbol{\Pi}_{2N}^{\text{in}} \end{aligned} \tag{15}$$

$$\boldsymbol{X}_{2N\times 2N} = \begin{bmatrix} \left[\text{diag}\left(\sqrt{N_{mn}k_{mn}/(2\rho_0 c_0 k)}\right)\right]_{N\times N} & \boldsymbol{0}_{N\times N} \\ t & \boldsymbol{0}_{N\times N}\left[\text{diag}\left(\sqrt{N_{mn}k_{mn}/(2\rho_0 c_0 k)}\right)\right]_{N\times N} \end{bmatrix} \quad (16)$$

The expression (10) becomes:

$$W_{\text{dis}} = \boldsymbol{\Pi}_{2N}^{\text{in}\,T^*}\left[\boldsymbol{I}_{2N\times 2N} - \boldsymbol{H}_{2N\times 2N}\right]\cdot\boldsymbol{\Pi}_{2N}^{\text{in}} \quad (17)$$

$$\boldsymbol{H}_{2N\times 2N} = \boldsymbol{S}'^{T^*}_{2N\times 2N}\cdot\boldsymbol{S}'_{2N\times 2N} \quad (18)$$

$$\boldsymbol{S}'_{2N\times 2N} = \boldsymbol{X}_{2N\times 2N}.\boldsymbol{S}_{2N\times 2N}\cdot\boldsymbol{X}^{-1}_{2N\times 2N} \quad (19)$$

The determination of eigenvalues and eigenvectors of the matrix $\boldsymbol{H}$ allows having a physical interpretation of the phenomena of the energy generation and absorption [23].

$$\boldsymbol{H}_{2N\times 2N} = \boldsymbol{U}_{2N\times 2N}\cdot\boldsymbol{\Lambda}_{2N\times 2N}\cdot\boldsymbol{U}^{T*}_{2N\times 2N} \quad (20)$$

with $\boldsymbol{U}$ and $\boldsymbol{\Lambda}$, respectively, matrices of eigenvectors and eigenvalues of $\boldsymbol{H}$, Eq. (10) becomes:

$$W_{\text{dis}} = \boldsymbol{d}^{T^*}_{2N}\cdot\left[\text{diag}\,(1-\lambda_i)\right]_{2N\times 2N}\cdot\boldsymbol{d}_{2N} \quad (21)$$

λ_i are the eigenvalues of the matrix $\boldsymbol{H}$.

The acoustic dissipation is then obtained:

$$W_{\text{dis}}(\text{Watts}) = \sum_{i=1}^{2N}(1-\lambda_i)|d_i|^2 \quad (22)$$

$$\boldsymbol{d}_{2N} = \boldsymbol{U}^{T^*}_{2N\times 2N}\cdot\boldsymbol{\Pi}^{\text{in}}_{2N} \quad (23)$$

The acoustic power dissipation in dB is given by the following expression:

$$W_{\text{dis}}(dB) = 10\log_{10}\left(W_{\text{dis}}(\text{Watts})/10^{-12}\right) \quad (24)$$

This development shows that the total acoustic power dissipation depends on the acoustic and geometric properties of the duct studied represented by its multimodal scattering matrix and the vector of incident modal pressures from the left and right sides of the element duct.

The acoustic power attenuation is defined as the ratio between the acoustic incoming and outgoing powers. It can also be deduced from the eigenvectors and eigenvalues of $\boldsymbol{H}$:

$$W_{\text{att}}(dB) = 10\log_{10}(W^{\text{in}}/W^{\text{out}}) = 10\log_{10}\left(\sum_{i=1}^{2N}|d_i|^2\Big/\sum_{i=1}^{2N}\lambda_i\,|d_i|^2\right) \quad (25)$$

The acoustic power attenuation also depends on the scattering matrix of the element duct under test and incident pressures.

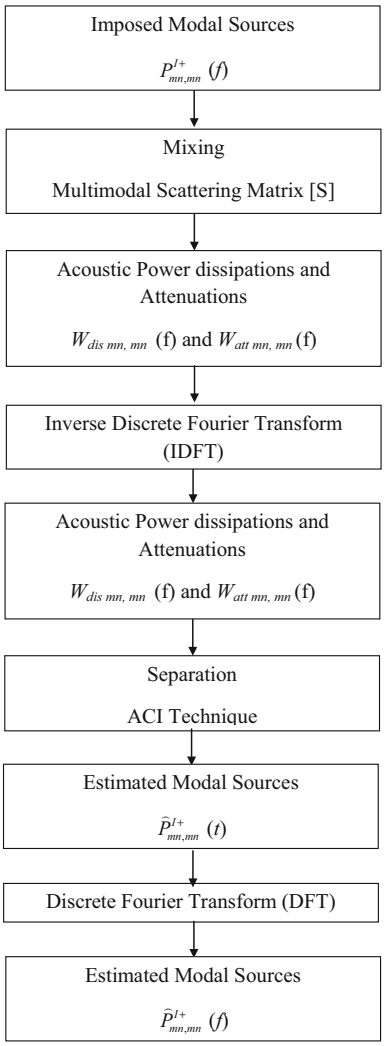

Fig. 2 Principle of the proposed reconstruction method using the ICA technique

4 Independent Components Analysis Method

The independent component analysis method (ICA) is one of the statistical methods of blind source separation techniques. Its objective is to decompose a random multivariable signal $\boldsymbol{x}(t)$ into a linear combination of statistically independent signals. This is expressed by the following equation [15–18,25,26] :

$$\boldsymbol{x}(t) = \boldsymbol{A}\boldsymbol{s}(t) \tag{26}$$

$\boldsymbol{x}(t) = \langle x_1, \ldots\ldots, x_M \rangle^T$ and $\boldsymbol{s}(t) = \left\langle s_1, \ldots\ldots, s_{N_s} \right\rangle^T$ are, respectively, the vector containing the observed signals and signal sources to be identified, M represents the number of observations, N_s is the number of sources, $M \geq N_s$ and $\boldsymbol{A}_{M \times N_s}$ is the unknown mixing matrix. The only known quantity is the vector of observations $\boldsymbol{x}(t)$. The ICA method has as objective to estimate the mixing matrix $\boldsymbol{A}$ and the source signals s_i with some indeterminacy to due to perturbations. The vector of observations can be written as follows:

$$\boldsymbol{x}(t) = \boldsymbol{A}\boldsymbol{D}^{-1}\boldsymbol{D}\boldsymbol{x}(t) \tag{27}$$

Table 1 Characteristics of studied point acoustic sources

Source	A_s (Pa)	θ_s (rad)	z_s (m)
S_1	0.2	$\frac{\pi}{3}$	−0.1
S_2	0.5	$\frac{\pi}{2}$	0.1

$\boldsymbol{D}$ is the diagonal matrix of the eigenvalues of the matrix $E(\boldsymbol{x}\boldsymbol{x}^*)$.

To apply the ICA method, few hypotheses must be met to ensure effective separation procedure. In fact, the sources must statistically independent, uncorrelated and non-Gaussian [24,26–28].

In order to extract the different sources from an unknown mixture, the ICA method requires some pretreatments for the observed signals: The first is that observed signals must be centered, i.e., subtracts its mean vector $m = E(\boldsymbol{x})$. So each signal becomes a zero-mean variable, and as result a zero-mean source signal is obtained. Secondly, the observations must be whitening, i.e., the measured signals $\boldsymbol{x}$ become white signals $\tilde{\boldsymbol{x}}$ with uncorrelated components and a variance equal to the unity [26]:

$$\tilde{\boldsymbol{x}} = \boldsymbol{W}\boldsymbol{x} \tag{28}$$

Here, $\boldsymbol{W}$ is the whitening matrix determined by the eigenvalue decomposition of the observed signals covariance matrix:

$$\boldsymbol{W} = \boldsymbol{D}^{-1/2}\boldsymbol{U}^T \tag{29}$$

where $\boldsymbol{U}$ is the orthogonal eigenvectors matrix.

In order to extract the source signals, the ICA method is based on the determination of each column of the separating matrix $\boldsymbol{B}$ in order to estimate N_s source signals defined by the vector $\boldsymbol{y}(t) = \langle y_1(t), \ldots.., y_{N_s}(t) \rangle^T$ as follows:

$$\boldsymbol{y}(t) = \boldsymbol{B}\boldsymbol{x}(t) \tag{30}$$

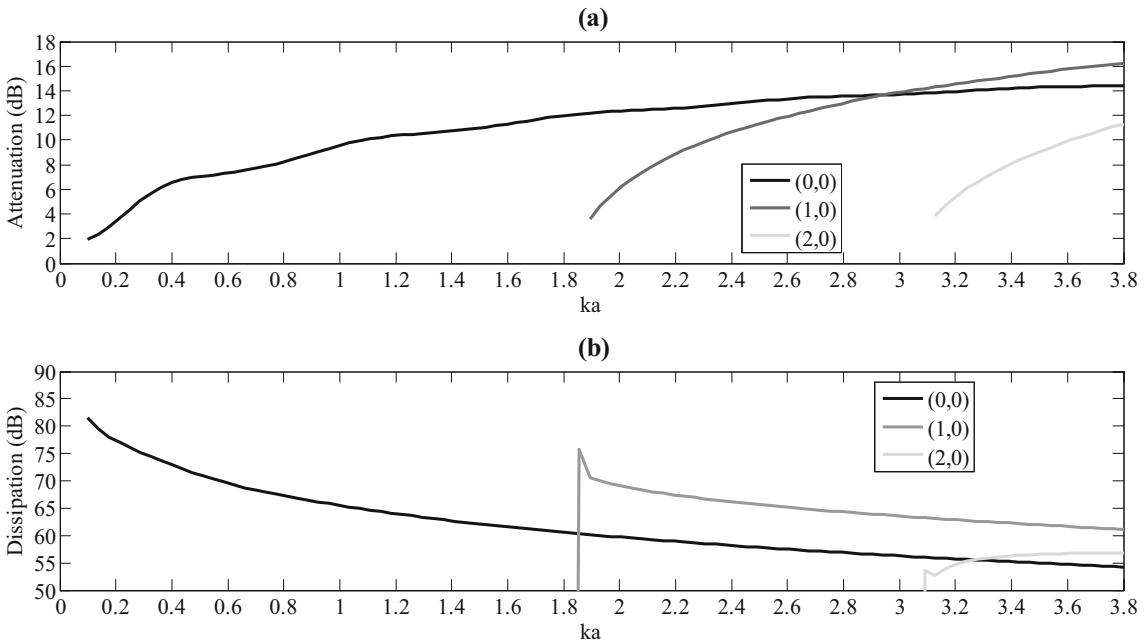

Fig. 3 Modal acoustic power attenuations (**a**) and dissipations (**b**) of the studied duct element in the case of the first point acoustic source S_1

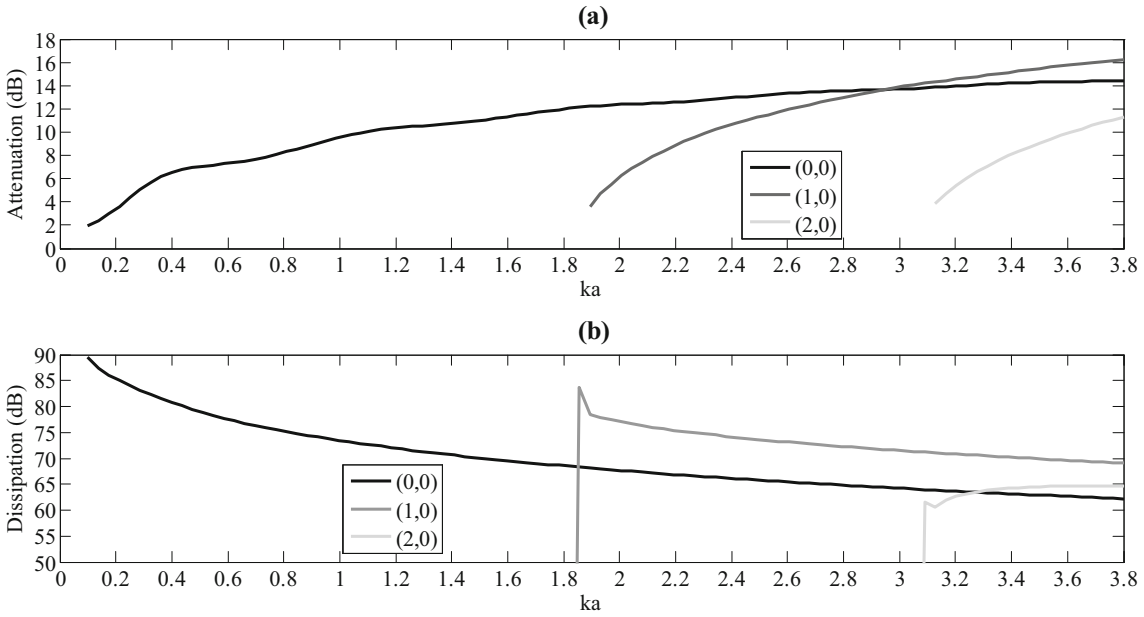

Fig. 4 Modal acoustic power attenuations (**a**) and dissipations (**b**) of the studied duct element in the case of the second point acoustic source S_2

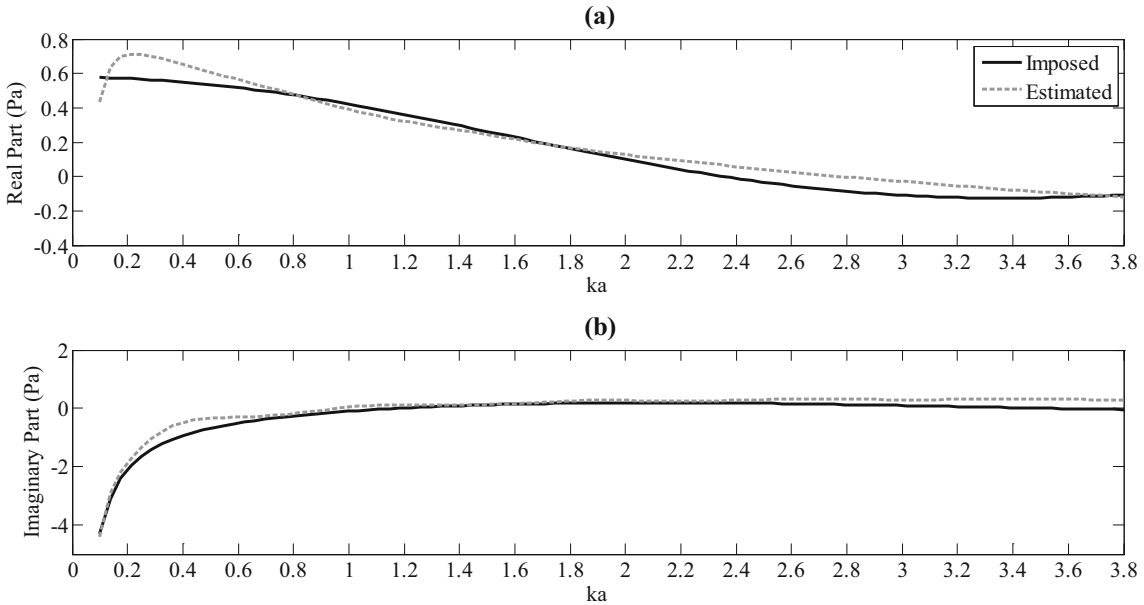

Fig. 5 A comparison between the estimated and imposed real part (**a**) and imaginary part (**b**) of the modal acoustic pressure emitted by the first point acoustic source S_1 corresponding to the mode (0,0)

The separating matrix $\boldsymbol{B}$ must maximize a contrast function in order to guarantee a non-Gaussianity distribution. The used contrast function is the Kurtosis which is defined by Zarzoso and Comen [29] as the normalized fourth-order marginal cumulate:

$$K(\text{ka}) = \frac{E\{|y|^4\} - 2E^2\{|y|^2\} - |E\{y^2\}|^2}{E^2\{|y|^2\}} \tag{31}$$

After determining the first column of the separating matrix, the ICA method exploited the deflation approach in order to extract the estimated sources from the original mixture related to the determined column of the separating matrix, so that each source will be chosen once with multiplying exact factor [27].

For the present study, as presented in Fig. 2, the modal acoustic power dissipations and attenuations $W_{\text{dis}\,nm,nm}(f)$ and $W_{\text{att}\,nm,nm}(f)$ are computed using the vector of incom-

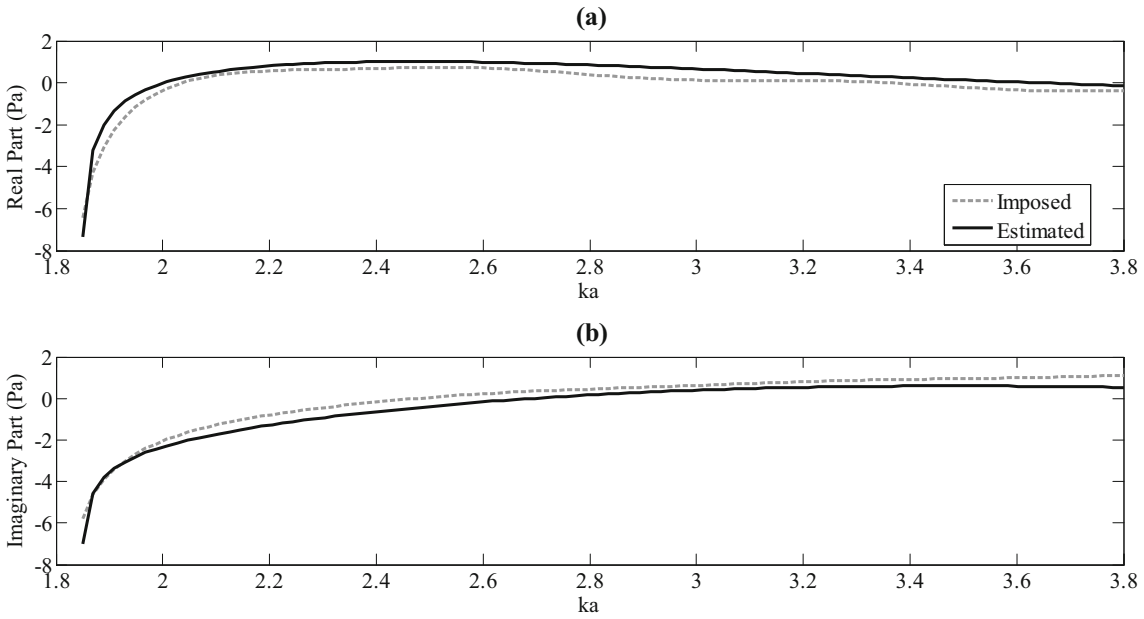

Fig. 6 A comparison between the estimated and imposed real part (**a**) and imaginary part (**b**) of the modal acoustic pressure emitted by the first point acoustic source S_1 corresponding to the mode (1,0)

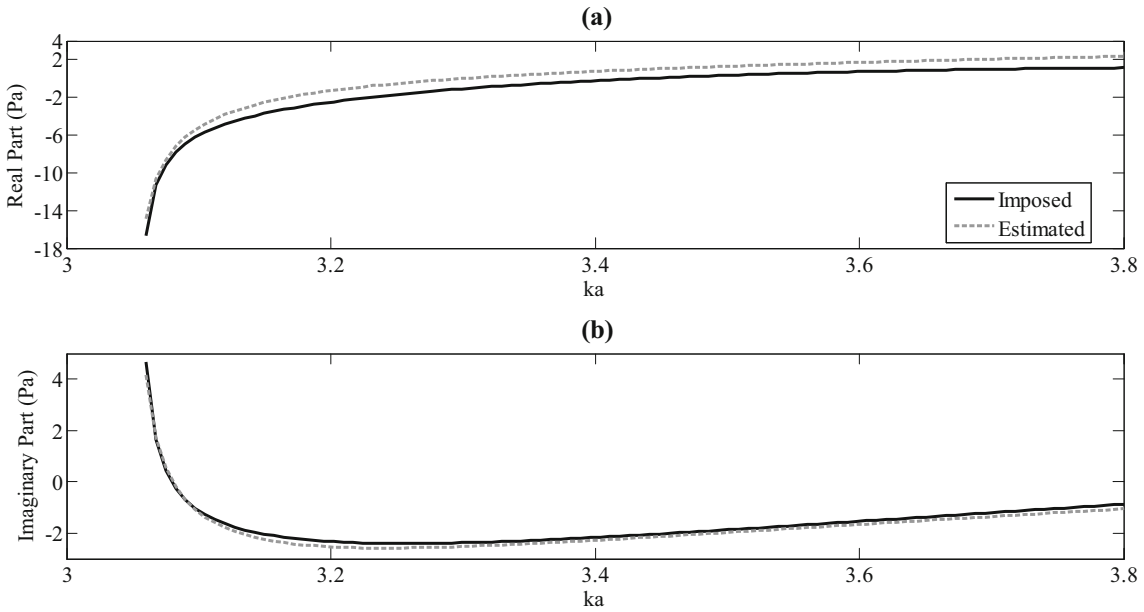

Fig. 7 A comparison between the estimated and imposed real part (**a**) and imaginary part (**b**) of the modal acoustic pressure emitted by the first point acoustic source S_1 corresponding to the mode (2,0)

ing modal pressures $P^{I+}_{mn,mn}(f)$ emitted by the point acoustic source defined by the expression (6). By using the Inverse Discrete Fourier Transform (IDFT), these quantities are changed from the frequency domain to the time domain to obtain $W_{\text{dis}\,nm,nm}(t)$ and $W_{\text{att}\,nm,nm}(t)$. The obtained time-dependent energetic quantities are then used as inputs to the ICA method to reconstruct the modal acoustic source pressures $P^{I+}_{mn,mn}(t)$. Then, by using the Discrete Fourier Transform (DFT), the estimated modal pressures $P^{I+}_{mn,mn}(f)$ are deduced.

5 Numerical Results

Two source configurations are used with the studied duct element. Table 1 presents the different characteristics of these

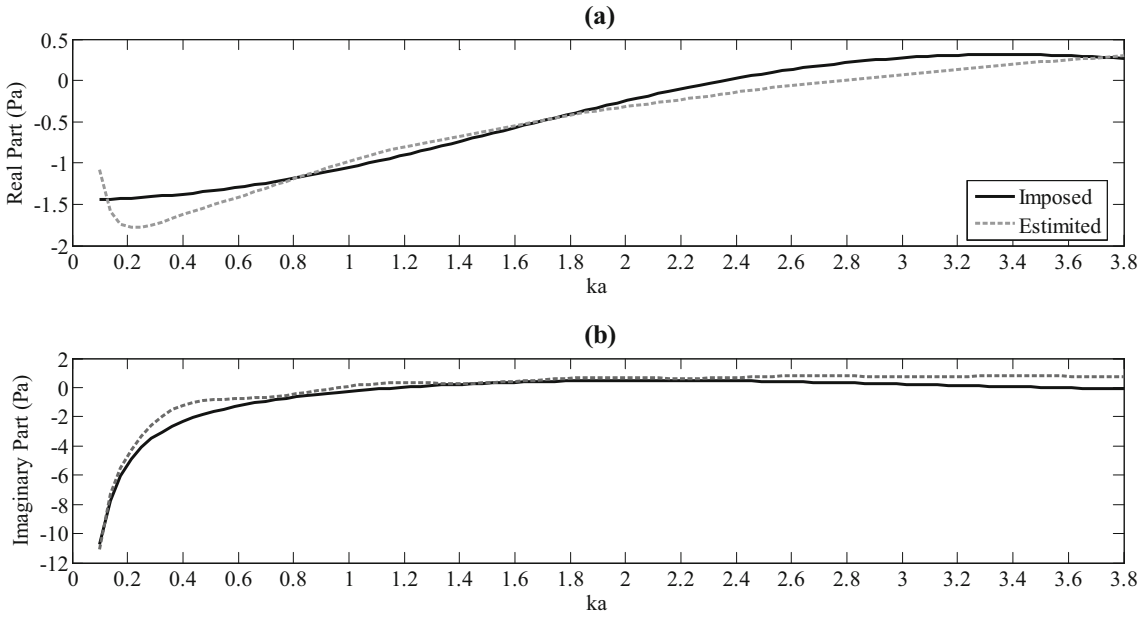

Fig. 8 A comparison between the estimated and imposed real part (**a**) and imaginary part (**b**) of the modal acoustic pressure emitted by the second point acoustic source S_2 corresponding to the mode (0,0)

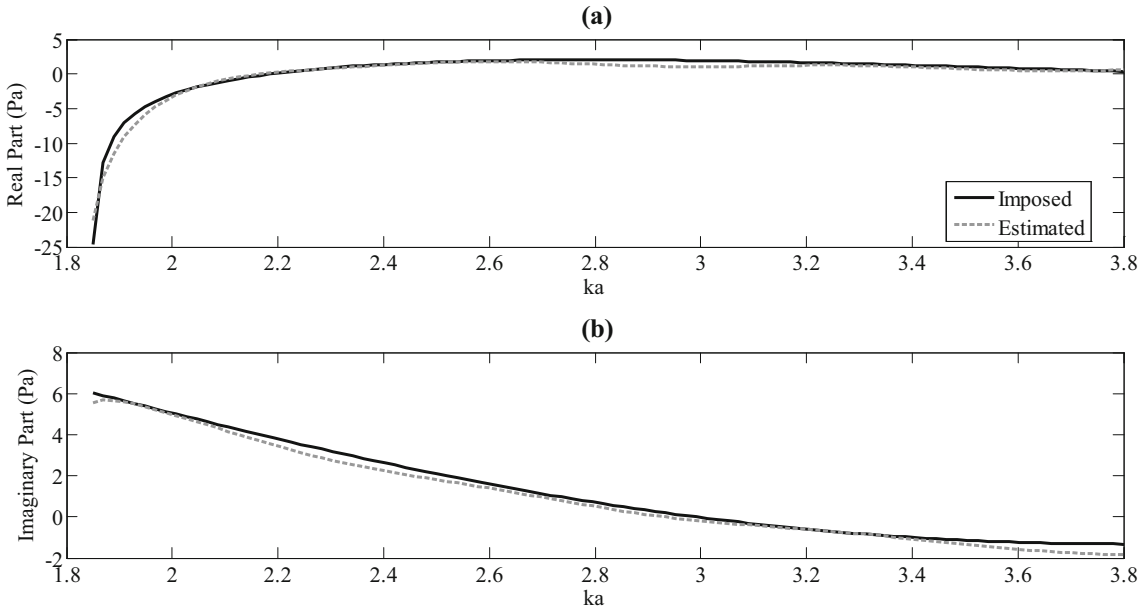

Fig. 9 A comparison between the estimated and imposed real part (**a**) and imaginary part (**b**) of the modal acoustic pressure emitted by the second point acoustic source S_2 corresponding to the mode (1,0)

point sources. For the two studied cases, we suppose that $\varphi_s = 0$.

To reconstruct the modal acoustic pressures emitted by the source, the corresponding modal attenuation and dissipation are used to estimate this pressure for each mode by using the development presented in Sect. 4. Figures 3 and 4 present these modal dissipations and attenuations versus ka $= [0 - 3.8]$, respectively, for the first and the second studied acoustic point sources. The five modal acoustic pressures present in this frequency band are uncoupled because using wall ducts at each side of the studied duct [30].

Because of the geometry of the studied duct (cylindrical), the modes $(-1,0)$ and $(-2,0)$ have the same effect than modes (1,0) and (2,0). So, only results corresponding to modes (0,0), (1,0) and (2,0) are presented and discussed.

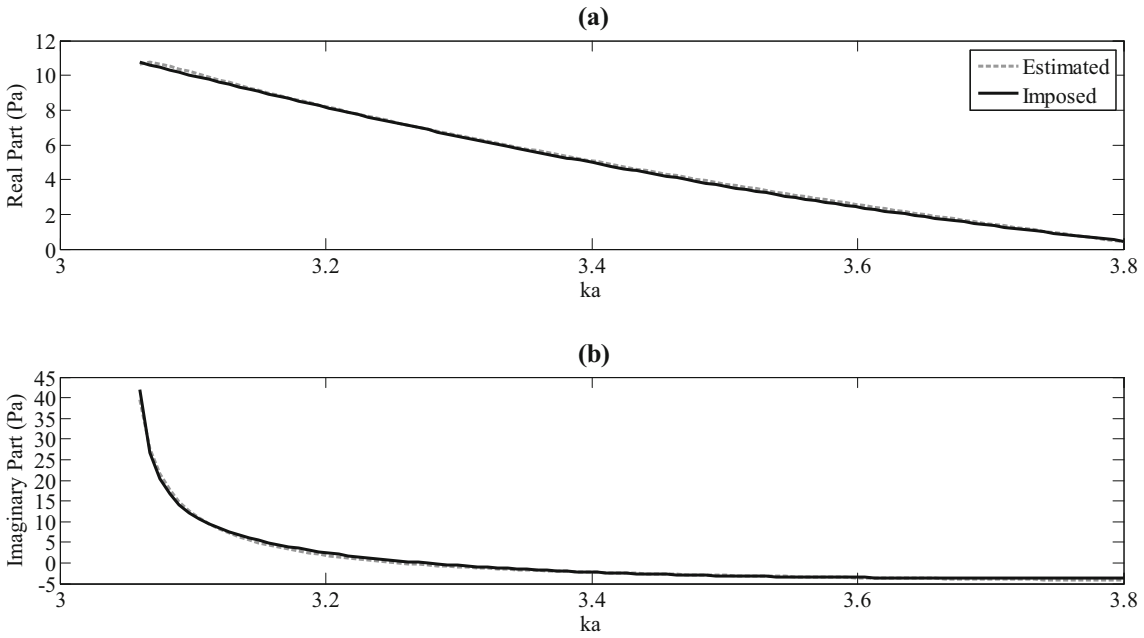

Fig. 10 A comparison between the estimated and imposed real part (**a**) and imaginary part (**b**) of the modal acoustic pressure emitted by the second point acoustic source S_2 corresponding to the mode (2,0)

Figures 5 to 7 present the comparison between the imposed and the estimated modal pressure emitted by the first point acoustic source, respectively, for the modes (0,0), (1,0) and (2,0). Figs. 8 to 10 present the same results in the case of the second point acoustic source. Figure indexed (a) presents the real part of the acoustic pressure when Fig. indexed (b) presents the imaginary part of the acoustic pressure. From these Figs, it is noticed that the estimated modal acoustic pressures are very close to the imposed modal pressure. So from these results, we can confirm that the proposed reconstruction method gives good results and allows recovering the imposed sources closely to the original source, whereas the mode and the frequency.

6 Conclusion

In this paper, an acoustic source reconstruction method is presented based on one of the major techniques of the blind source separation which is the independent component analysis. In fact, this work is focused on estimating the modal pressure emitted by a point source in duct systems knowing only energetic parameters presenting by the acoustic power dissipations and attenuations. By applying the developed method for a studied case, the results of the reconstruction show the efficiency of this technique. Thus, the independent component analysis represents a useful method based on a separation sources algorithm used for identifying the acoustic sources applied on duct systems. Experimental results can be used as inputs of this technique for real cases.

Appendix

The acoustic pressure inside a cylindrical duct is given by:

$$P(r,\theta,z,t) = \sum_{m=-\infty}^{+\infty} \sum_{n=0}^{+\infty} P_{mn}(z)\Psi(r,\theta)e^{-i\omega t} \tag{A1}$$

P_{mn} are the modal coefficients associated with the mode (m,n). These coefficients are defined by:

$$P_{mn}(z) = \frac{\langle P|\Psi_{mn}\rangle}{N_{mn}} \tag{A2}$$

Ψ_{mn} are the transversal eigenmodes given by:

$$\Psi_{mn}(r,\theta) = J_m\left(\frac{\chi_{mn}r}{a}\right)e^{\mathrm{i}m\theta} \tag{A3}$$

The orthogonality of transversal eigenmodes in a hard wall duct was demonstrated by Auger [31]. It is expressed as follows:

$$\langle\Psi_{pq}|\Psi_{mn}\rangle = \int_S \Psi_{mn}(r,\theta)\Psi^*_{pq}(r,\theta)dS = \begin{cases} N_{mn} & \text{if } (m,n) = (p,q) \\ 0 & \text{if } (m,n) \neq (p,q) \end{cases} \tag{A4}$$

with N_{mn} is the normalization factor associated with the mode (m,n):

$$N_{mn} = \langle \Psi_{mn} | \Psi_{mn} \rangle = \begin{cases} N_{00} = 1 \\ N_{mn} = S J_m^2(\chi_{mn}) \left(1 - \frac{m^2}{\chi_{mn}^2}\right) \end{cases} \quad \text{(A5)}$$

References

1. Hewlett, D.A.K.; Nelson, P.A.: A model based approach for estimating the strength of acoustic sources within a circular duct. In: Second AIAA/CEAS Aeroacoustics Conference. State College, PA (1996)
2. Nelson, P.A.; Yoon, S.H.: Estimation of acoustic source strength by inverse methods: part I, conditioning of the inverse problem. J. Sound Vib. **233**, 643–668 (2000)
3. Nelson, P.A.; Yoon, S.H.: Estimation of acoustic source strength by inverse methods: part II, experimental investigation of methods for choosing regularization parameters. J. Sound Vib. **233**, 669–705 (2000)
4. Kim, Y.; Nelson, P.A.: Estimation of acoustic source strength within a cylindrical duct by inverse methods. J. Sound Vib. **275**, 391–413 (2004)
5. Kim, Y.; Nelson, P.A.: Spatial resolution limits for the reconstruction of acoustic source strength by inverse method. J. Sound Vib. **265**, 583–608 (2003)
6. Kim, Y.; Nelson, P.A.: Optimal regularization for acoustic source reconstruction by inverse methods. J. Sound Vib. **275**, 463–487 (2004)
7. Schumacher, A.; Hald, J.; Rasmussen, K.B.; Hansen, P.C.: Sound source reconstruction using inverse boundary element calculations. J. Acoust. Soc Am. **113**, 14–127 (2003)
8. Bravo, T.; Maury, C.: In-duct acoustic source reconstruction from pressure and velocity-based measurements. In: 13th AIAA/CEAS Aeroacoustics Conference. Rome (2007)
9. Maury, C.; Bravo, T.: Analytic solution to the acoustic source reconstruction problem. Proc. R. Soc. Lond. Ser. A **464**, 1697–1718 (2008)
10. Bravo, T.; Maury, C.: Microphone array beamforming and inverse methods for the reconstruction of ducted acoustic sources. In: 14th International Congress on Sound and Vibration. Cairns (2007)
11. Bravo, T.; Maury, C.: Inverse source strength reconstruction techniques for ducted acoustics sources. In: 15th International Congress on Sound and Vibration. Daejeon (2008)
12. Maury, C.; Bravo, T.: Experimental feasibility of in-duct sound source reconstruction Acoustics' 08. Paris, pp. 1773-1778 (2008)
13. Bravo, T.; Maury, C.: Enhancing the reconstruction of in-duct sound sources using a spectral decomposition method. J. Acoust. Soc. Am. **127**(6), 3538–3547 (2010)
14. Zhong, D.; Yang, D.; Zhu, M.: Localization of sound source within a finite length duct with beamforming methods. In: 20th International Congress on Sound and Vibration. Bangkok (2013)
15. Abbès, M.S.; Miladi, M.; Akrout, A.; Fakhfakh, T.; Haddar, M.: Vibratory behavior of a double panel system by the operational modal analysis. Int. J. Model. Simul. Sci. Comput. **2**(4), 459–479 (2011)
16. Taktak, M.; Tounsi, D.; Akrout, A.; Abbès, M.S.; Haddar, M.: One stage spur gear transmission crankcase diagnosis using the independent components method. Int. J. Veh. Noise Vib. **8**(4), 387–400 (2012)
17. Akrout, A.; Tounsi, D.; Taktak, M.; Abbès, M.S.; Haddar, M.: Estimation of dynamic systems excitation forces by the independent component analysis. Int. J. Appl. Mech. **4**(3), 1250032 (2012)
18. Akrout, A.; Tounsi, D.; Taktak, M.; Abbès, M.S.; Haddar, M.: Inverse method for a gear spur diagnosis. J. Appl. Theor. Mech. **53**(3), 617–628 (2015)
19. Taktak, M.; Ville, J.M.; Haddar, M.; Gabard, G.; Foucart, F.: An indirect method for the characterization of locally reacting liners. J. Acoust. Soc. Am. **127**(6), 3548–3559 (2010)
20. Akoum, M.; Ville, J.M.: Measurement of reflection matrix of a discontinuity in a duct. J. Acoust. Soc. Am. **103**(5), 2463–2468 (1998)
21. Sitel, A.; Ville, J.M.; Foucart, F.: Multiload procedure to measure the acoustic scattering matrix of a duct discontinuity for higher order mode propagation conditions. J. Acoust. Soc. Am. **120**(5), 2478–2490 (2006)
22. Ville, J.M.; Foucart, F.: Experimental set up for measurement of acoustic power dissipation in lined ducts for higher order modes propagation with air mean flow conditions. J. Acoust. Soc. Am. **114**(4), 1742–1748 (2003)
23. Aurégan, Y.; Starobinski, R.: Determination of acoustical energy dissipation/production potentiality from the acoustical transfer functions of a multiport. Acta Acust United Acust **85**, 788–792 (1999)
24. Comon, P.: Separation of sources using higher-order cumulates. In: Actes of Advanced Algorithms and Architectures for Signal Processing IV, vol. 1152, pp. 170–181, California (1989)
25. Thi, H.L.N.; Jutten, C.: Blind source separation for convolutive mixtures. Signal Process. **45**, 209–229 (1995)
26. Hyvärinen, A.; Oja, E.: Independent component analysis: algorithms and applications. Neural Netw. Res. Cent. Hels. Univ. Technol. **13**(4-5), 411–430 (2000)
27. Antoni, J.: Blind separation of vibration components: principles and demonstration. Mech Syst. Signal Process. **19**, 1166–1180 (2005)
28. Moreau, E.; Macchi, E.: New self-adaptive algorithms for source separation based on contrast functions. In: Actes of Work on Higher-Order Statistics (HOS'93), pp. 215–219. Lake Tahoe (1993)
29. Zarzoso, V.; Comon, P.: Robust independent component analysis by iterative maximization of the kurtosis contrast with algebraic optimal step size. IEEE Trans. Neural Net. **21**(2), 248–261 (2010)
30. Bi, W.P.; Pagneux, V.; Lafarge, D.; Aurégan, Y.: Modelling of sound propagation in a non-uniform lined duct using a multi-modal propagation method. J Sound Vib. **289**, 1091–1111 (2006)
31. Auger, J.M.: Méthode de mesure de la structure modale du champ acoustique dans un conduit cylindrique par double transformée de Fourier-Lommel avec ou sans écoulement. Thesis in the University of Technology of Compiègne, France (1987)

Robust ASR Systems using Auditory Filter in Impulsive Noise Environment

Issam Bel Haj Yahia
Research Laboratory of Signal Image and Information Technology (RLSIIT) National Engineering School of Tunis, TUNISIA

Zied Hajaiej
Research Laboratory of Signal Image and Information Technology (RLSIIT) National Engineering School of Tunis, TUNISIA

ABSTRACT
This paper is dedicated to the development of new automatic methods for recognizing of isolated words with impulsive sounds. This article presents a parameterization technique of speech signal with impulsive noise based on auditory filter modeling by the gammachirp filterbank (Gammachirp Filter Banc (GFB). This work includes two parts; the first is devoted to traditional techniques. The second deals with modern methods incorporating a model of auditory filter called gamma chirp. In this section, we will extract the characteristics of a single word with impulsive noise from the TIMIT database using parameterization technique Perceptual Linear Preduction(PLP) with the GFB.The recognition system is implemented on Hidden Markov Model Toolkit HTK platform based on HMM. For evaluation a comparative study was operated with standard PLP and Mel Frequency Cepstral Coefficient (MFCC). We propose a study of the performance of new parameterization technique GFB_PLP and GFB_MFCC proposed in the presence of different impulsive noises. Three types of impulsive noise are used (blast door, glass breaks, and explosion) Tests were carried out at different SNR levels (15dB, 10dB, 5dB, 0 dB and -3 dB) The GFB –PLP technique give the better results in different tests.

General Terms
Impulsive noise ,gammachirp ,asr recognition

Keywords
Mfcc, plp, gfb mfcc, gfb plp

1. INTRODUCTION
speech is a natural mode of communication for humans. It isvery efficient, for transmission of information conversational speaking rates can be as high as 200 words perminute. And for reception of information, has others advantages as well. Speech recognition is today a quite common element in our lives. Cellular phones, computers, telephone services and many more products use speech recognition. An important drawback affecting most of the speech processing systems is the environmental noise and its harmful effect on the system performance. The presence of noise normally degrades the performance of speech recognition; therefore it is very important that a speech recognizer in some way deals with possible noise. A large amount of work has therefore been spent in this area and there exists a lot of technique that improves the speech recognizer'smodels are generally a filterbank, none uniformly spaced in frequency and with non-uniform bandwidths, narrows at low frequencies, and broad at high frequencies, which converts the input speech signal into a performances in noisy conditions. Signal theory tools for representation of signals and systems in the time domain or in the spectral domain, their study and analysis, modeling and interpretation. Detecting the absence or presence of a signal, signal with a noise and speech recognition are treated frome problems. Indeed, the natural sounds are composed of noise, and the ear is sensitive to information related to this part [8]. With this noisy component, which is considerate for several years, we present the different characteristics of the noise part.The purpose of this article is to introduce several important concepts in signal processing and illustrate them with relatively simple examples. At first, to focus on the study and analysis of impulsive noise by incorporating a model auditory filter called gammachirp [1][3]. In this paper, we propose a techniques for parameterization speech signals based on a gammachirp filterbank (GFB) following the approach used in the technical PLP. For this we will develop a system for automatic recognition of isolated words with impulsive noise based on Hidden Markov Models HMM, the recognition system will serve as an evaluation of the impulsive signal by gammachirp filter. We propose a study of the performance of parameterization technique GFB_PLP and GFB_MFCC proposed in the presence of different impulsive noises. The sounds are added to the word with different snr (15dB, 10dB, 5dB, 0 dB and --3 dB). The recognition performance of this approach was evaluated using theTIMIT database.The obtained evaluation results are compared to thos of the standards techniques. .

2. SPEECH RECOGNITION SYSTEMS ASR
The speech recognition system has two major components, feature extraction and classification. In this work the system block diagram of isolated word recognition is shown in Figure1.

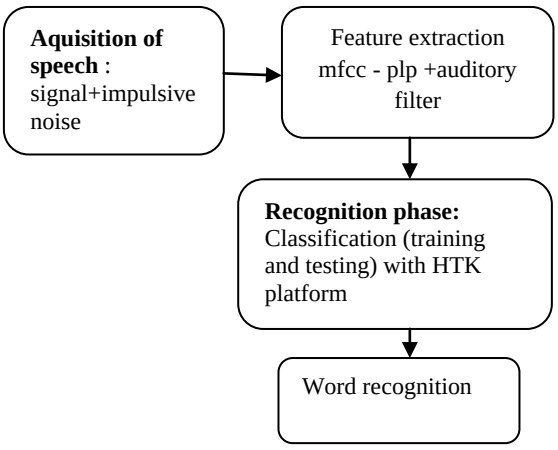

Fig 1: Structure of asr System.

3. PERCEPTUAL LINEAR PREDICTION (PLP)

Perceptual linear prediction analysis is a variation of the original LPC analysis and was first introduced by Hermansky [7] in 1990. The main idea of this technique is to take advantage of three principal characteristics derived from the psychoacoustic properties of the human ear for estimating the audible spectrum. This concept is Spectral resolution of the critical band, Equal-loudness curve and Intensity loudness power law. The audible spectrum is then approximated from an all pole autoregressive model. The PLP analysis is nearer to the behavior of the human ear than the traditional LPC technique. This last characteristic renders this method more robust in speaker-independent conditions. The PLP analysis is however computationally efficient and permits a compact representation of speech. The method considers the short term power spectrum of speech and makes a convolution of it with a simulated critical band masking pattern. Then, the critical-band is re sampled at about one Bark scale intervals. At this point, a preemphasis operation is performed with a fixed equalloudness curve and finally the resulting spectrum is compressed with cubic-root nonlinearity, simulating the intensity-loudness power law. The resulting low order all pole models is consistent with several phenomena observed in human speech perception. In this step, the IDFT (Inverse Discrete Fourier Transforms) is applied to obtain the dual autocorrelation function. The first M+ 1 values are used for solving the Yule-Walker [13] equation for obtaining the autoregressive coefficients of the all-pole model of order M [21] [2].

4. MEL FREQUENCY CEPSTRAL COEFFICIENT (MFCC)

The cepstral coefficients are derived from the output of the Mel filter bank formed from triangular filters and positioned uniformly across Mel. This technique consists in calculating the cepstral coefficients on a Mel scale that approximates the frequency perception of the ear. After applying a Fourier transform in the short term, energy is calculated in critical heath modeled by triangular filters when the amplitude scale is expressed in decibels. The frequency scale in turn is expressed in Mel. Then the Inverse Cosine Transform (IDFT) provides lesser correlated coefficients. The cepstrum is then given by the fol-lowing expression:

$$C_n = \sqrt{\frac{2}{k}} \sum_{k=1}^{N} \left(\log S_k \cos\left[n\left(k - \frac{1}{2} \right) \frac{\pi}{k} \right] \right)$$

Sk : representing the energy after filtering by a k triangular filter

5. AUDITORY GAMMACHIRP FILTER

The gammachirp filter is used in the psychoacoustic research as a reliable model of cochlear filter. The gammachirp filter is defined in the time domain (impulse response function) as:

$$gc(t) = a^{n-1} \exp(-2\pi b ERB(f_r)\, t) \exp(j2\pi f_r + jc \ln t + jc\varphi)$$

a: an amplitude normalization parameter.

c: a parameter for the chirp rate.

b: a parameter defining the envelope of the gamma distribution.

ERB (fr): Equivalent Rectangulaire Bandwith.

φ : the original phase.

The gammachirp to be expressed as the cascade of a gammatone filter with an asymmetric compensation filter. Figure 2 shows the framework for this cascade approach.

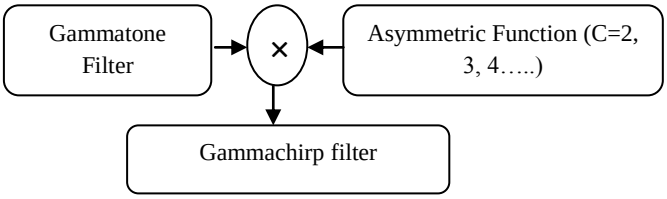

Fig 2: Decomposition of the gammachirp filter

The gammachirp filter which is derived out of the gammatone filter modification was introduced to model the asymmetry in the low frequency tail of the auditory filter response and to model level dependent proprieties such as decrease in gain, bandwidth increase and a shift in the center frequency of the filter with increase in level. Where time t>0, a is the amplitude, (fr) is the asymptotic frequency and b are parameters defining the envelope of the gamma distribution. C is a parameter for the frequency modulation or the chirp rate, φ is the initial phase, and ERB (fr) represents the Equivalent Rectangular Bandwidth of the filter, given by the following relationship:

$$ERB(f_r) = 24.7 + 0.108 f_r$$

The Fourier transform of the gammachirp in is derived as follows

$$G_c(f) = \frac{a|\Gamma(n+jc)|}{\Gamma(n)} \cdot \frac{\Gamma(n)}{\left|2\pi\sqrt{(b.ERB(f_r))^2 + (f - f_r)^2}\right|^n} e^{C\theta}$$

$$|G_c(f)| = a_\Gamma |G_T| . e^{C\theta(f)}$$

$$\theta(f) = \arctan\left(\frac{f - f_r}{bERB(f_r)} \right)$$

Gc (f) is the Fourier magnitude spectrum of the gammatone filter, e cθ (f) is an asymmetric function since it antisymmetric function centered at the asymptotic frequency. The spectral properties of the gammachirp will depend on the e cθ (f), factor; this factor has therefore been called the asymmetry factor. The degree of asymmetry depends on "c". If "c" is negative, the transfer function, considered as a low pass filter, where c is positive it behaves as a high-pass filter and if "c" zero, the transfer function, behaves as a gammatone filter. In addition, this parameter is connected to the signal power (Ps)by the expression

$$C = 3.38 + 0.107\, Ps$$

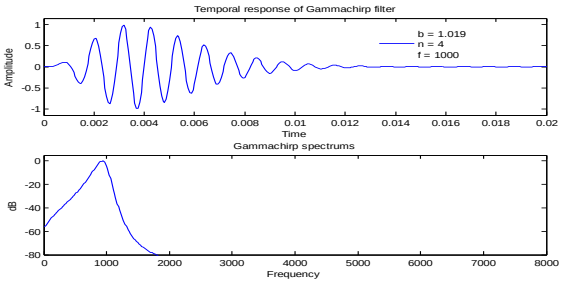

Fig 3: Example of Impulse Response Gammachirp

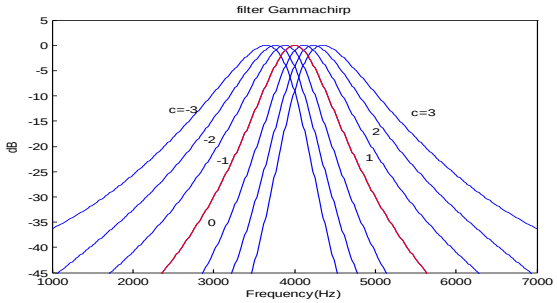

Fig 4: Gammachirp spectrums for different values of c

The figure 5 shows a block diagram of the gammachirp filterbank

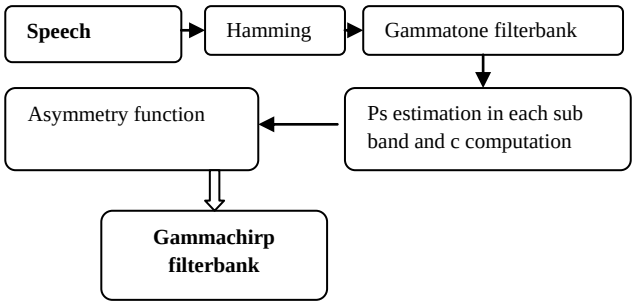

Fig 5: Block diagram of the gammachirp filterbank

The figure 6 shows the algorithm of PLP and the GFB-PLP parameterization

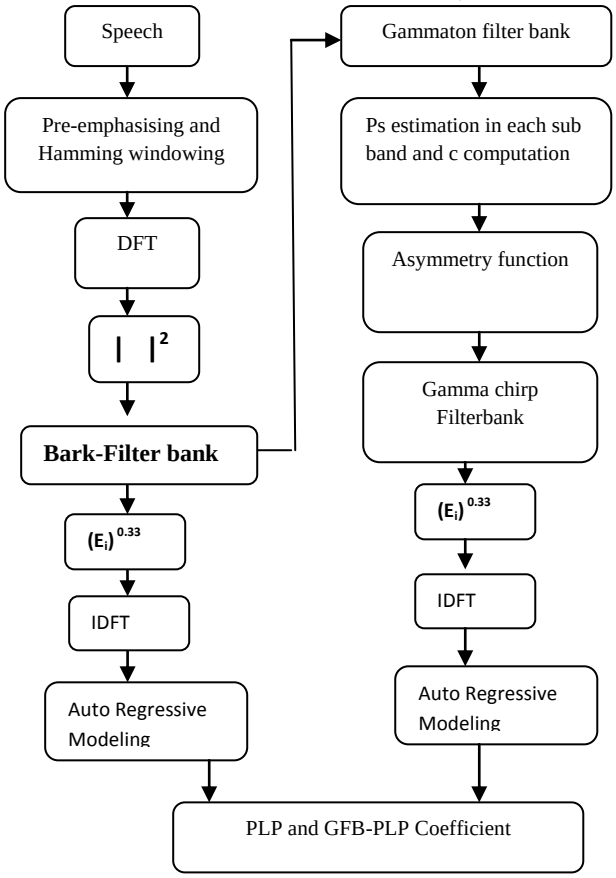

Fig 6: Block diagram of PLP and the gfb-plp parameterization

The object of the GFB-PLP analysis is to estimate coefficients by an auditory model of a filter based on filter bank whose gammachirp. The algorithm calculates GFB-PLP coefficient is based on the same step of calculated PLP coefficient in that, we only change the Bark filter bank by gammachirp filter.

The figure 7 shows the algorithm of MFCC and the GFB-MFCC parameterization

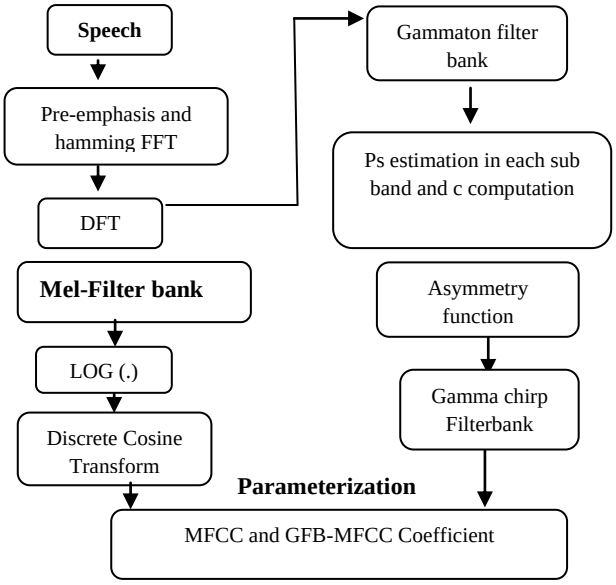

Fig 7: Block diagram of mfcc and the gfb-mfcc

The object of the GFB-MFCC analysis is to estimate coefficients by an auditory model of a filter based on filter bank whose Gamma chirp. The algorithm calculates GFB-MFCC coefficient is based on the same step of calculated MFCC coefficient in that,we only change the mel filter bank by gammachirp filter .

6. EXPERIMENTS CONDITIONS

In this paper to evaluate the GFB-PLP parameterization technique, we carried out a comparative study with different baseline parameterization techniques of MFCC and PLP implemented in HTK We tested the performance in speech signal recognition tasks wehre the training database is clean and the test database contaminated with additive impulsive noise different real-environment impulsive noises used: blast door, glass breaks, and explosion provided by Tests were carried out at different SNR levels (15dB, 10dB, 5dB, 0 dB and -3 dB).

6.1 Timit Database

The training database is built of several words extracted from the Darpa-Timit database (8). This database is composed of speech composed of 8 American dialects. We used 6132 words composed of 21 words (models) repeated 292 times from 36 speakers (18 males and 18 females) uniformly divided for American dialects. For the test phase of recognition we used 2201 words from 26 speakers (13 males and 13 females).[15][16].

6.2 Impulsive Noise

Impulsive noise consists of relatively short duration, caused by a variety of sources for example explosions and gunshots, human screams, door slams, glass breaks, dog barks, phone rings, machine noise, pieces of music or children voice sounds. In our work we used three class of impulsive noise: explosions, glass breaks, and door slams. Impulsive noise is usually non-stationary, non-Gaussian and very complex frequency behavior. It is for this reason that we are interested in the study of the noise. The duration of this noise is low in the order of second, theory feature is a Dirac. As the example in Figure 2 and 3 gives time representation and spectrogram of door slam impulsive noise.

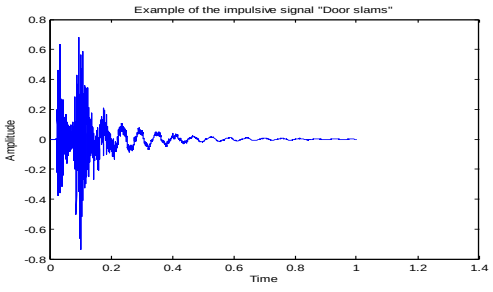

Fig 7: Time representation of door slam impulsive noise

System description

Features used in our test Mel-frequency cepstral coefficients MFCC. Another popular feature set is the set of perceptual linear prediction (PLP) coefficients. The 39-element feature vector contains 12 MFCC or PLP or GFB-PLP or GFB-MFC C(implemented in HTK platform), one energy measure, and their first and second derivatives. In our experiment, there were 21 HMM models (21Recognized words) trained using the selected feature (GFB-PLP, MFCC PLP and GFB-MFCC). The observation probabilities are modeled as a weighted sum of Gaussian probability densities. The system uses 21 models (words). Each speech model is represented by an HMM with 5 by 5 states,from left-to-right (the first and the last ones are non-emitting) and 12 mixture components per state [10]. In the Training Process parameters of HMM are estimated during a supervised process using a maximum likelihood approach with Baum-Welch re-estimation. The first step in determining the parameters of an HMM is to make a rough guess about their values. Then, the Baum-Welch algorithm is applied to these initial values to improve their accuracy in the maximum likelihood sense. Finally, The Viterbi decoding algorithm is used in the decoding process. The recognition problem is to find a state sequence of a model which is most likely to have been generated by the data. The Viterbi decoding algorithm assumes that the maximum likelihood state sequence travels through the optimal path along each state [6].

6.3 Recognition Results

In this section we present the different results obtained for the parameterization techniques, GGB-PLP, MFCC,GFB-MFCC and PLP. The performance is tested on the TIMIT databases using HTK. The features vectors consist of GFB-PLP. Each one consists of 12 cepstrals coefficients and energy (E), concatenated with the delta (D) and acceleration (A) coefficients. The features vectors are of dimension 39. The performance is compared with the MFCC, PLP, GFB-MFCC and GFB-PLP baseline as the same condition. Tables 1, 2, 3 and 4 show the average recognition accuracy.

Table 1. Words recognition accuracy rate for clean speech

	Brut	**e**	**e-d**	**e-d-a**
Mfcc	91	93.14	98.14	99.05
plp	91. 46	93.68	98.15	99.35
Gfb-plp	90.12	93.43	97.56	98.93
Gfb-mfcc	93.05	49.22	98.66	99.85

Table 2. Words recognition accuracy rate for blast door impulsive noise

	-3db	**0db**	**5db**	**10db**	**15db**
Mfcc (e-d-a)	35.67	65.79	90.55	97.68	98.82
Plp(e-d-a)	32.06	65.4	91.33	97.18	98.14
Gfb-plp(e-d-a)	32.05	65.11	90.11	97.21	98.17
Gfb-mfcc(e-d-a)	40.17	68.54	91.11	98.6	98.96

Table 3. Words recognition accuracy rate for glass breaks impulsive noise

	-3db	**0db**	**5db**	**10db**	**15db**
Mfcc (e-d-a)	37.55	59.6	88.87	97.32	98.36
Plp(e-d-a)	36.44	57.7	98.23	97.73	97.96
Gfb-plp(e-d-a)	35.5	55.4	87.36	59.38	98.8
Gfb-mfcc(e-d-a)	39.40	66.98	84.55	98.77	99.14

Table 4. Words recognition accuracy rate for blast door impulsive noise

	-3db	0db	5db	10db	15db
Mfcc (e-d-a)	63.43	87.85	97.36	98.6	98.82
Plp(e-d-a)	60.11	88.37	97.77	97.27	98.14
Gfb-plp(e-d-a	59.00	86.33	97.10	97.10	98.9 6
Gfb-mfcc(e-d-a)	66.30	89.97	98.80	98.27	99.5

6.4 Discussion

From these results it can be seen that the GFB –MFCC technique give the better result (highest accuracy of recognition) 99.85% in clean speech with add energies of signal and derived parameters.

In noise speech it can be seen that the system's highest accuracy of recognitions 98.96% and 99.50% are obtained for GFB-PLP techniques in blast door and explosion, impulsive noise. With -5db SNR level. In tables 2, 3 and 4 the technique GCFB-PLPgive the better result is 40.17%, 39.40%, and 66.3% respectively with -3db SNR level.

We notice that the GFB-MFCC technique gives acceptable results in all the experience.

7. CONCLUSION

In this work, we evaluated the new technique of parameterization of the speech signals GFB- PLP (who takes account of the characteristics frequential and temporal of the ear, based on a filter bank gammachirp GFB and a classic MFCC PLP and (GFB -PLP techniques in clean and noise environment with different SNR levels (15dB, 10dB, 5dB, 0 dB and -3 dB).

The results gotten after application of this features show that this method (GFB-PLP, GFB-MFCC) give acceptable and better results by comparison at those gotten by other methods of parameterization.

We used the platform HTK toolkit, that use Hidden Markov Models and we used the TIMIT speech databases and impulsive noise in our evaluations. The results obtained after application of Gammachirp filter on the word show that this filter gives acceptable and sometimes better results.

In other issues of this work, the following strategy is applied to improve different obtained results

- Testing the state efficiency of HMM approach
- Raising the filter numbers in different techniques
- increase for example the number of coefficients in the parameters techniques

8. REFERENCES

[1] Timo Gerkmann, Richard C. Hendrikes, "Noise power estimation based on the probability of speech presence," Proc. IEEEWASPAA, pp. 145-148, New York, Oct. 2011.

[2] Irino. T, E. Okamoto, R. Nisimura, Hideki Kawahara and Roy D. Patterson, "A Gammachirp Auditory Filterbank for Reliable Estimation of Vocal Tract Length from both Voiced and Whispered Speech," The 4th Annual Conference of the British Society of Audiology, Keele, UK, 4-6, Sept, 2013

[3] T. Irino, R. D. Patterson. ''Temporal asymmetry in the auditory system.'' J. Acoust. Soc. Am. 99(4): 2316-2331, April, 1997.

[4] T. Irino, R. D. Patterson. ''A time-domain, Level-dependent auditory filter: The gammachirp.'' J. Acoust. Soc. Am. 101(1): 412-419, January, 1997.

[5] T. Irino et M. Unoki. ''An Analysis Auditory Filterbank Based on an IIR Implementation of the Gammachirp.'' J. Acoust. Soc Japan. 20(6): 397-406, November, 1999.

[6] Patterson, R, D., Nimmo-Smith, I., ''Off-frequency listening and auditory-filter asymmetry'' J. Acoust. Soc. Am, Vol. 67, No. 1, pp. 229-245, 1980.

[7] SCHLÜTER, R., BEZRUKOV, I., WAGNER, H., NEY, H, "Gamma tone features and feature combination for large vocabulary speech recognition," In ICASSP 2007. Honolulu (HI, USA), April 2007, p. 649-652.

[8] Paliwal, K, K., "Decorrelated and Liftered Filter-Bank Energies for Robust Speech Recognition", Proc. Eurospeech, pp. 85-88. 1999.

[9] Irino, T., Patterson, R, D., ''A compressive gammachirp auditory filter for both physiological and psychophysical data.'' J. Acoust Soc. Am. 109(5): 2008-2022, may 2001.

[10] Young, S., Evermann,G., Gales, M., Hain, T. D., Kershaw,X. Liu, Moore, G., Odell, J. D., Ollason, D., and Woodland. P., The HTK book (for HTK version 3.4). Cambridge University Engineering Department, Cambridge, UK, 2006.

[11] Young S. J., Woodland P. C., Byrne W. J., "HTK. Reference Manual for HTK version 3.1", December 2001.

[12] L.R. Rabiner. A tutorial on hidden Markov models and selected applications in speech processing. Proceedings of IEEE, 77(2):257–286, 1989.

[13] Zied Hajaiej, Kais Ouni, Noureddine Ellouze, " Etude et évaluation d'une technique de paramétrisation perceptive des signaux de parole ", Traitements & Analyse d'Informations : Méthodes & Applications, TAIMA 05, Hammamet, Tunisie, pp.259 – 264, 1–3 octobre 2005.

[14] Smith III, J, O., Abel, J, S,. ''Bark and ERB Bilinear Transforms.'' IEEE Tran. On speech and Audio Processing, Vol. 7, No. 6, November 1999.

[15] NIST., The DARPA TIMIT Acoustic-phonetic Continuous Speech Recognition Database, 1990 .

[16] Hermansky, H., ''Perceptual Linear predictive (PLP) analysis of speech'', J. Acoust. Soc. Am. Vol. 87, No. 4, pp. 1738-1752., April 1990

[17] Varga, A., Steeneken, H,J,M., Omlison, M,T., Jones, D., "The NOISEX-92 Study on the Effect of Additive Noise on Automatic Speech Recognition", Documentation included in the NOISEX-92 CD-ROM Set.,1992

[18] A. B. Poritz, "Hidden Markov models: A guided tour", in Proc. of the IEEE Int'l. Conf. on Acoustics, Speech and Signal Processing (ICASSP '88), May 1988, pp. 7-13.

[19] E. Loweimi and S. M. Ahadi, "A new group delay-based feature for robust speech recognition," in Proc. IEEE

Int. Conf. on Multimedia & Expo, Barcelona, pp. 1-5, July 2011.

[20] Skowronski M. D. and Harris J. G., 2002, "Increased MFCC filter bandwidth for noise-robust phoneme recognition", in Proc. ICASSP-02, Florida.

[21] L. Bréhélin, O. Gasuel. « Modèles de Markov cachés et apprentissage des séquences. Le temps, l'espace et l'évolutif en sciences du traitement de l'information », Éditions Cépaduès, pp. 407-421, 2000.

[22] Zied Hajaiej, Kaïs Ouni and Noureddine Ellouze "Gammachirp Filter Frond-End for Automatic Speech Recognition "International Conference: Sciences of Electronic, Technologies of Information and Telecommunications SETTIT, 2000

mit-polytech.tn

Design Your life